Åbo Akademi

Mathias Nyman

Interfacial Effects in Organic Solar Cells

Interfacial Effects in Organic Solar Cells

Mathias Nyman

Physics
Center for Functional Materials
Faculty of Science and Engineering
Åbo Akademi University
Åbo, Finland, 2015

Supervisor

Prof. Ronald Österbacka
Åbo Akademi University

Pre-Examiners

Assoc. Prof. Attila Mozer
University of Wollongong

Docent Janne Halme
Aalto University School of Science

Opponent for the public defense

Prof. Ellen Moons
Karlstad University

ISBN 978-952-12-3169-8
Painosalama Oy – Turku, Finland 2015

Table of contents

Preface

The work presented in this thesis was carried out under the supervision of Professor Ronald Österbacka in the group of molecular electronics at the Department of Physics, Åbo Akademi University between the years 2008 and 2014. This work was made possible thanks to generous funding from the Academy of Finland, the Magnus Erhnrooth foundation and the The Society of Swedish Literature in Finland.

In the spring of 2006 Ronald asked me if I would be interested in writing my master's thesis on organic solar cells. I agreed and conducted the work over the following two years. Without me even quite realizing what was going on, I was hired on a three year Academy of Finland project starting in 2008, and have continued doing research since then. I would like to thank Ronald for his knowledgeable supervision of this work, and for having faith in me despite the occasionally slow progress.

Research in natural sciences nowadays is largely a collaborative effort; the work presented here would not have been possible without the valuable input of my co-authors. Special thanks go to Dr. Harri Aarnio for teaching me how to make solar cells and Oskar Sandberg for providing theoretical insight to my results. I would also like to thank all my colleagues in the molecular electronics group and the personnel at the physics department. I have had the opportunity of taking part in a lot of international collaboration, for which I am grateful.

Lastly I would like to thank my family and friends for their support, and Inka-Maria for her endless encouragement and love.

Åbo 23.01.2015

Mathias Nyman

List of included publications

This thesis is based on the following publications. The publications are included in the end of the thesis with permission from the publishers.

Paper I *Origin of Equilibrium Charges in Poly(3-hexylthiophene):[6,6]-phenyl-C61-butyric acid methyl ester Solar Cell Devices*
M. Nyman, F. Pettersson, and R. Österbacka
Chemical Physics **404** 60–63 (2012)

Paper II *Voltage dependent displacement current as a tool to measure the vacuum dipole shift caused by self assembled monolayers on aluminum oxide*
M. Nyman, O. J. Sandberg, J. F. Martínez Hardigree, S. Kola, H. E. Katz, and R. Österbacka
*Appl. Phys. Lett.***103**, 243502 (2013)

Paper III *The Effect of Degradation on the Active Layer in APFO3:PCBM Solar Cells*
M. Nyman, H. Aarnio, S. Mühlbach, U. Würfel, and R. Österbacka
Energy Procedia **31** 26-30 (2012)

Paper IV *The Effect of Contacts in Bulk Heterojunction Solar Cells*
O. J. Sandberg, M. Nyman, and R. Österbacka
Phys. Rev. Appl. **1**, 024003 (2014)

Paper V *2D- and trap-assisted 2D-Langevin Recombination in Polymer:Fullerene Blends*
M. Nyman, O. J. Sandberg and R. Österbacka
Adv. Energy Mater. (in press)
doi: 10.1002/aenm.201400890

Author's contribution

Paper I The author planned and executed all the experimental work except the Kelvin probe measurements and wrote the paper together with R. Österbacka.

Paper II The author planned and executed all the CELIV measurements on devices prepared by J. Martinez Hardigree and wrote the paper together with the co-authors. The analytical derivations were done by O. J. Sandberg.

Paper III The author planned and executed all the measurements on devices prepared by S. Mühlbach and wrote the paper together with the co-authors.

Paper IV The author participated in the planning of the work carried out by O. J. Sandberg and in the interpretation of the results, and finalized the paper together with the co-authors.

Paper V The author planned and executed all the experimental work and wrote the paper together with the co-authors. The analytical derivations were done by O. J. Sandberg.

List of additional publications

Paper 1 *Spontaneous Charge Transfer and Dipole Formation at the Interface Between P3HT and PCBM*
H. Aarnio, P. Sehati, S. Braun, M. Nyman, M. P. de Jong, M. Fahlman, and R. Österbacka
Adv. Energy Mater. **1** 5 792 (2011)

Paper 2 *Charge Transport Studies on Novel PT-derivatives with Hydrophilic Anchoring Groups*
M. Nyman, K. Akitsu, N. Otani, M. Matsamura, T. Kubo, H. Segawa, and R. Österbacka
Synth. Met. **164** 60-63 (2013)

Paper 3 *Reducing Leakage Currents in Organic Field-effect Transistors Using Molecular Dipole Monolayers on Nanoscale Oxides*
J. F. Martínez Hardigree, T. J. Dawidczyk, R. M. Ireland, G. L. Johns, B.-J. Jung, M. Nyman, R. Österbacka, N. Marković, and H. E. Katz
ACS Appl. Mater. Interfaces **5** (15), 7025–7032 (2013)

Paper 4 *Direct Determination of Doping Concentration and Built-in Voltage from Extraction Current Transients*
O. J. Sandberg, M. Nyman, and R. Österbacka
Org. Electron. **15** (2014) 3413–3420

Paper 5 *Charge transport in intercalated and non-intercalated polymer:fullerene blends*
M. Nyman, O. J. Sandberg, and R. Österbacka
Synth. Met. (in press) doi: 10.1016/j.synthmet.2015.01.010

1. Introduction

1.1. Background

The field of organic electronics has seen tremendous research efforts during the last few decades. The much improved understanding of the underlying physical processes such as charge transport and recombination, in addition to significant progress in material synthesis and characterization has led to vastly improved device performance [1]. Organic light emitting diodes (OLED) have already been commercialized and are presently ubiquitously used in both small and large-sized displays. Organic field effect transistors (OFET) are on the verge of commercialization and performance currently exceeds amorphous silicon with charge carrier mobilities exceeding 10 cm^2/Vs [1]. The field of OFET research is rapidly breaking new ground in biosensing and bioelectronics [2,3].

The field of organic photovoltaics (OPV) is also advancing at a fast rate, the power conversion efficiencies (PCE) of OPV cells are increasing at a rate of approximately 1-2% annually [4] and the 10 % mark has been exceeded. However, the certified efficiencies are typically measured on 1 cm^2 large devices, and scale-up to large panels is still challenging; additional research is still needed in order to increase performance and cut production costs. Furthermore an improved understanding of degradation processes is needed in order to increase the life span of OPV based cells.

To date, most of the research efforts in organic electronics have been focused around improving the physical understanding and properties of the bulk of the active materials. However, recently Braun et al demonstrated that the interfaces between different domains in the device are also of great importance, owing to the fact that the surfaces and interfaces of disordered organic materials can have distinctly different properties than the bulk [5].

1.2. Solar cells

Chapin, Fuller and Pearson presented what is commonly referred to as the first practical solar cell in 1954 [6]. The cell was based on Silicon and had an efficiency of ~ 6 %. The working principle of a solar cell is as follows (see Figure 1.2.1); an incident photon is absorbed in the photoactive semiconductor if the photon energy is higher than the bandgap (E_g) of the semiconductor. This excites an electron from the valence band to the conduction band leaving a positively charged hole in the valence band. The electron and hole are then extracted at the contacts to the outer circuit.

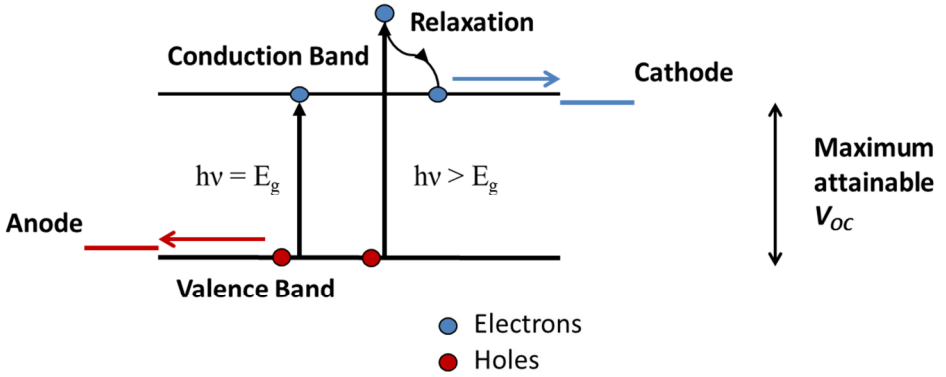

Figure 1.2.1 Schematic of the working principle of a solar cell.

The power conversion efficiency (*PCE*) is defined as:

$$PCE = \frac{J_{SC}V_{OC}FF}{P_{light}} \times 100\ \% \qquad (1.2.1)$$

where J_{SC} = the short circuit current, V_{OC} = the open circuit voltage, *FF* = the fill factor and P_{light} is the power of the light source. *FF* is defined as the ratio between the red small rectangle and the blue large rectangle in Figure 1.2.2. A small E_g is desirable in order to absorb as many photons as possible, however, for photons with $h\nu > E_g$ the extra energy is lost to thermodynamical relaxation. In general, assuming solar light generation, the lower the bandgap the higher the J_{SC} and the lower the V_{OC}, hence there is some optimal bandgap that maximizes the product of the J_{SC} and the V_{OC}. Shockley and Queisser derived, using the principle of detailed balance, the maximum achievable efficiency for a single junction solar cell at room temperature to be ~ 44 % (the detailed balance or Shockley-Queisser limit) and the optimal bandgap to be ~ 1.1 eV [7]. Taking further losses into account they furthermore showed that the highest attainable *PCE* for a single junction cell is ~ 31 % under practical circumstances.

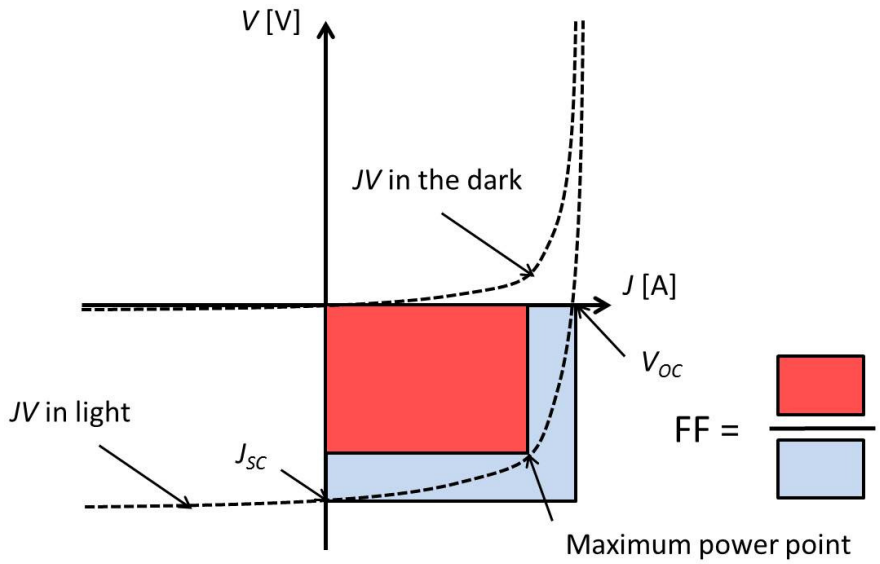

Figure 1.2.2 Schematic of a solar cell *JV* curve in dark and in light.

1 .3. Organic donor-acceptor systems

OPV offers the possibility of cost-efficient and large volume production of solar cells due to the fact that organic materials can be processed from solution which allows for low temperature and high throughput production methods such as roll-to-roll printing [4]. Although tremendous progress has been made in the field the power conversion efficiencies still need to be increased.

Organic semiconductors are disordered and have weak dielectric screening compared to inorganic ones. This means that free charges cannot readily be created upon photoexcitation, instead a vibronically excited state is created. Initial attempts at replacing inorganic materials with organic in solar cells were unsuccessful due to the high exciton binding energy in organic materials [8]. Furthermore, organic semiconductors are typically highly disordered which implies that the electronic states are strongly localized, as opposed to crystalline inorganic semiconductors such as silicon. As a result of the localized nature of the electronic states, the energy levels in organic materials do not form energy bands but a density of localized states located around the highest occupied molecular orbital (HOMO) and the lowest unoccupied molecular orbital (LUMO) for holes and electrons, respectively. The charge transport thus occurs around the HOMO level (E_{HOMO}) for holes and the LUMO level (E_{LUMO}) for electrons.

In 1986, Ching Tang discovered that the light generated exciton can be split into a hole and an electron by introducing another material with an energetically

lower lying LUMO level in a so called bi-layer device [9]. In this case light is absorbed in the donor material and if the energy offset between the LUMO levels of the bi-layer materials is large enough the exciton binding energy is overcome and the electron is transferred to the acceptor. However, the *PCE* was still very modest, around 0.5 %. The fact that the exciton diffusion length is rather short (around 10 nm) means that only the excitons generated close to the bi-layer junction will result in free electrons and holes thus limiting the J_{SC}.

A second breakthrough was reached in 1995 by Yu et al. They showed that two materials with different electron affinities can be blended into a so called bulk heterojunction (BHJ) thereby greatly increasing the donor-acceptor interface [10]. The phase separation of the two materials is of great importance, the domain size should be roughly twice the exciton diffusion length. Furthermore, both materials should have a conducting pathway across the whole film since the electrons are transported to the contacts in the acceptor and the holes in the donor. The morphology of these bulk heterojunction blends can be modified by annealing, choice of solvent and so on [11]. A BHJ can be seen as one effective semiconductor with $E_{HOMO} = E_{HOMO,D}$ and $E_{LUMO} = E_{LUMO,A}$ (defined as positive) with an effective band gap E_g^{DA} defined as:

$$E_g^{DA} = E_{HOMO,D} - E_{LUMO,A} \tag{1.3.1}$$

The BHJ concept allows for efficient generation of charges. However, the energy offset required between the LUMO levels of the donor and acceptor leads to lowered efficiencies. Janssen et al and Koster et al demonstrated, using similar detailed balance arguments as Shockley and Queisser, that the maximum attainable efficiency of organic BHJ solar cells is 20-24% [12, 13]. In order to achieve this, understanding of the relevant loss mechanisms is essential.

As discussed, the energy levels of the donor and acceptor materials needs to be chosen so that there is a sufficiently large energy offset between the donor and acceptor LUMO levels and the product of the J_{SC} and the V_{OC} is maximized. Furthermore, in order to achieve a high J_{SC} one also has to minimize the recombination. Recombination is the reverse process to generation, whereby electrons and holes meet in the bulk of the device and are eliminated. Recombination will be further discussed in section 2.2.

What determines the V_{OC} of BHJ solar cells has been debated extensively in the literature. From the splitting of the quasi-Fermi levels it follows that [14]:

$$qV_{OC} = E_g^{DA} - kT \ln\left(\frac{N_C N_V}{np}\right) \tag{1.3.2}$$

where q is the elementary charge, k_B is the Boltzmann constant, T is the temperature, n and p the density of electrons and holes and N_C and N_V the total amount of states in the conduction and valence band respectively. In the case of bi-molecular recombination it can be shown that $np = G/\beta$ yielding [14]:

$$qV_{OC} = E_g^{DA} - kT \ln\left(\frac{N_C N_V}{G/\beta}\right) \qquad (1.3.3)$$

where G is the generation and β the bi-molecular recombination coefficient. Furthermore, it has been shown experimentally that $qV_{OC} \approx E_g^{DA} - 0.3$ eV for a set of different donor-acceptor blends [15].

There is evidence that all charge generation and recombination goes via a so called charge transfer (CT) state [16, 17]. The CT state is a charge transfer complex that is formed at the donor-acceptor interface due to weak ground-state interaction (wave function mixing). A CT state implies partial charge transfer between one or more donor and acceptor molecules. Vandewal et al showed that the V_{OC} in BHJ solar cells is determined by the energetic position of the CT state [16]. It is not fully clarified exactly what determines the position of the CT state, but the interfacial properties of the donor and acceptor materials are clearly important.

1.4. Contacts

Good contacts are essential in order to have efficient extraction of the photo-generated charges. A contact is said to be Ohmic if an infinite amount of charges can be supplied from the metal to the semiconductor. The work function of a metal is defined as the minimum amount of energy required to remove one electron from the metal to vacuum. The requirement of an Ohmic contact is that the work function of the anode (cathode) is energetically close (roughly within kT) to the HOMO (LUMO) level of the organic semiconductor and that both the charge injection and charge extraction is sufficiently fast compared to the charge transport in the bulk. The rate at which charges are extracted from the device can be described using a surface recombination velocity [18]. If the surface recombination velocity is much smaller than the drift velocity of charge carriers in the bulk the contact will be extraction limited with the consequence that a space charge builds up at the contact. This will result in the appearance of an inflection point, or s-shape in the *JV* curve, significantly reducing the *FF*. In addition, an efficient solar cell should have selective contacts; an ideal cathode (anode) should be Ohmic for electrons (holes) and highly blocking for holes (electrons).

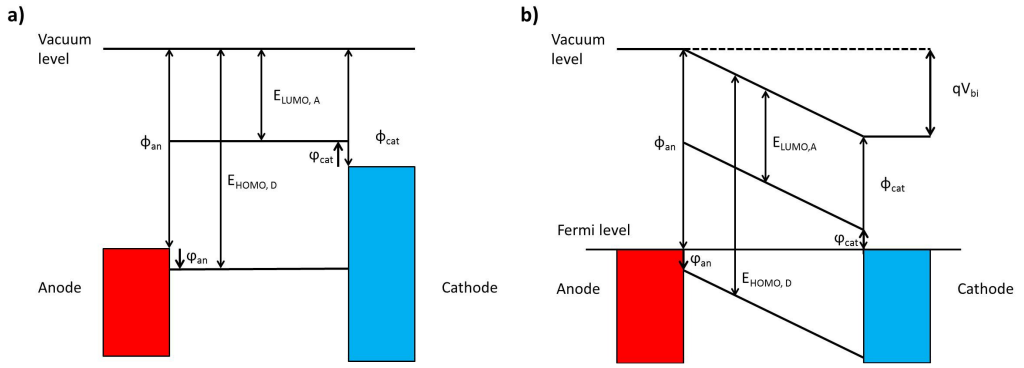

Figure 1.4.1 Schematic of the energy levels in a BHJ solar cell before (a) and after contact (b). $\phi_{an,cat}$ is the anode/cathode work function, $V_{bi} = (\phi_{an} - \phi_{cat})/q$ is the built-in voltage and φ_{an} and φ_{cat} is the injection barrier for holes at the anode and electrons at the cathode respectively.

Non-ideality of contacts may arise due to several different reasons, in addition to a low surface recombination velocity. If the HOMO of the donor lies lower in energy than the work function of the anode Φ_{an} there will be an electrostatic barrier $\varphi_{an} = E_{HOMO,\,D} - \Phi_{an}$ for injection of holes from the anode to the HOMO of the donor (see Figure 1.4.1). Correspondingly if the LUMO of the acceptor lies higher in energy than the work function of the cathode Φ_{cat} there will be a barrier for injection of electrons $\varphi_{cat} = \Phi_{cat} - E_{LUMO,\,A}$. Large injection barriers also typically result in s-shaped *JV*s greatly reducing device performance as illustrated in Figure 1.4.2 [19, 20, Paper IV].

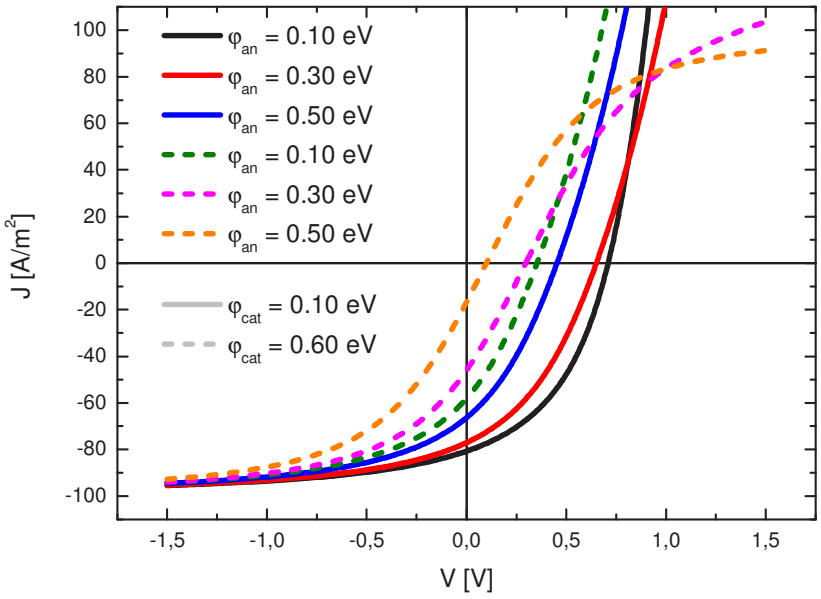

Figure 1.4.2 The effect of injection barriers at the contacts [Paper IV].

Doping of the active layer in the vicinity of the contacts can also result in an s-shape, if the doping density is high enough, due to the fact that the fixed space charge of the dopants screens the electric field [Paper IV]. In addition, non-ideal contacts can also result in a significantly reduced V_{OC}; taking non-ideal contacts into account the V_{OC} is given by [Paper IV]:

$$qV_{OC} = E_g^{DA} - \max(\varphi_{an}, \delta_p) - \max(\varphi_{cat}, \delta_n) \tag{1.4.1}$$

where $\delta_{n(p)}$ is approximately given by:

$$\delta_{n(p)} \approx \frac{kT}{2} \ln\left(\frac{\beta N_{c(v)}}{G}\right) + \frac{kT}{2} \ln\left(\frac{\mu_{n(p)}}{\mu_{p(n)}}\right) \tag{1.4.2}$$

under the assumption that $\mu_n n_{ph} \approx \mu_p p_{ph}$ where n_{ph} and p_{ph} is the density of photogenerated electrons and holes, respectively and $\mu_{n(p)}$ is the mobility of electrons(holes). The approximation breaks down at strongly imbalanced mobilities.

1.5. Degradation

When a BHJ device is operated or stored, the device performance will eventually decrease due to degradation of the device. In principle all components (contacts, interfacial layers and active layers) in a device are susceptible to degradation and in many cases several degradation mechanisms occur at the same time. This makes it complicated to determine the main cause of the reduced performance when comparing a degraded device to a pristine one. Degradation has been shown to reduce both the V_{OC} and J_{SC} [21, 22], but the perhaps most prominent feature of a degraded solar cell is an s-shaped *JV* curve. An s-shaped *JV* is usually attributed to non-ideality of the contacts as discussed above [18-20], however, other reasons such as imbalanced mobilities, doping of the active layer and unfavorable vertical phase separation have also been reported [22-25].

1.6. Aim

The energy levels of the active layers and electrodes play a crucial role in organic electronic devices. Furthermore, the interfaces between different layers have been shown to have distinctly different properties than the bulk materials due to impurities and different morphology. In order to further increase the performance and operational lifetimes of organic electronic devices interface engineering becomes increasingly important. The aim of this thesis is to clarify how interfacial effects affect the performance of organic diodes and solar cells. The relevant interfaces in this thesis are the contact-active layer interface (metal-organic) and the donor-acceptor interface (organic-organic). The effects of Fermi level alignment, charge trapping at contacts and reduced performance due to degradation are clarified using *JV* characterization, photo-induced absorption and the charge extraction by a linearly increasing voltage technique in addition with drift-diffusion simulations. Furthermore the effect of anisotropic charge transport and charge trapping on recombination is clarified using both transient and steady-state extraction techniques on polymer:fullerene blends with varying donor-acceptor stoichiometry. The measurement techniques employed are not in themselves surface-sensitive, however, since the interfacial properties have such a large impact on the transient and steady-state currents in these devices the techniques mentioned serve as efficient probes of the properties of the relevant interfaces.

2. Theory

2.1. Interface energetics

The energy levels of the active layers and electrodes play an important role in organic electronic devices. The HOMO and LUMO levels of the donor and the acceptor define the maximum attainable open circuit voltage in BHJ solar cells. In order to have efficient charge injection and charge extraction the work functions of the contact materials are also of crucial importance. However, lately the importance of the interfaces between different material components has become more and more evident [5]. The interfaces between different layers have been shown to have distinctly different properties than the bulk materials due to impurities and differences in morphology between surface and bulk [5]. Although the interfacial regions in general are small compared to the volume of the whole device, interfacial effects can hugely affect the operational performance of organic electronic devices. In thin film devices especially the interfaces play an increasingly important role, for instance it has been shown that band bending at the electrode active layer interface can stretch several tens on nanometers into the bulk of the active layer [26].

2.1.1. Metal-organic interface

Consider a metal with work function ϕ_{metal} (here defined as positive) in intimate contact with an organic semiconductor. If $E_{LUMO} > \phi_{metal}$ electrons will flow across the interface to the organic LUMO level (minimizing their energy) until the Fermi levels are aligned, effectively pinning the LUMO level of the organic material to the metal work function. Correspondingly holes will flow to the HOMO level of the organic material if $E_{HOMO} < \phi_{metal}$. This is known as Fermi level pinning and is effectively seen as a dipole shift of the vacuum level. If ϕ_{metal} is between the HOMO and LUMO levels no pinning will occur effectively creating an injection barrier for both electrons and holes. However, it has been shown by several groups that the Fermi level does not pin to the bulk HOMO and LUMO levels, since the surfaces and interfaces of organic materials can have distinctly different properties, but to a band of discrete interfacial states [5, 27]. The interfacial dipole caused by the Fermi level pinning are typically measured using surface sensitive measurements such as ultraviolet photoelectron spectroscopy (UPS) and x-ray photoelectron spectroscopy (XPS). While there is an agreement in the scientific literature that interfacial dipole formation occur the exact underlying mechanisms are still debated. One proposed model is the integer charge transfer (ICT) model. The ICT

model assumes that an integer amount of charge is transferred, as opposed to partial charge transfer.

2.1.2. The integer charge transfer model

The ICT model presented by Prof. Fahlman and co-workers is an attempt to clarify the mechanism of interfacial dipole formation caused by Fermi level pinning at weakly interacting interfaces. Examples of such interfaces are organic/organic interfaces and interfaces formed with substrates passivated by oxides or residual hydrocarbons [5]. The presence of oxides or hydrocarbons prevents the formation of interfacial dipoles via partial electron transfer, however, dipole formation is still possible via tunneling into well-defined states on the organic molecule. Tunneling implies the transfer of an integer amount of charge [5].

The energy of the positive integer charge transfer state (E_{ICT+}) is defined as the minimum energy required to remove one electron from the molecule producing a fully relaxed state. The energy of the negative integer charge transfer state (E_{ICT-}) is defined as the maximum energy gained when an electron is added to the molecule. Depending on the substrate work function (ϕ_{metal}) three different scenarios may arise when bringing the metal substrate in contact with the organic material (see Figure 2.1.1). If $\phi_{metal} > E_{ICT+}$ electrons will flow from the organic material into the substrate creating a vacuum level (dipole) shift Δ, this flow will continue until $E_{ICT+} + \Delta = \phi_{metal}$, hence the Fermi level will be pinned to the E_{ICT+} level (Figure 2.1.1 a)). If $\phi_{metal} < E_{ICT-}$ the opposite will occur, that is electrons will flow from the substrate into the organic material until $E_{ICT-} - \Delta = \phi_{metal}$ thereby pinning the Fermi level to the E_{ICT-} state (Figure 2.1.1 b)). Lastly, if $E_{ICT-} < \phi_{metal} < E_{ICT+}$ no electrons can flow across the interface and vacuum alignment will occur (Figure 2.1.1 c)) [5].

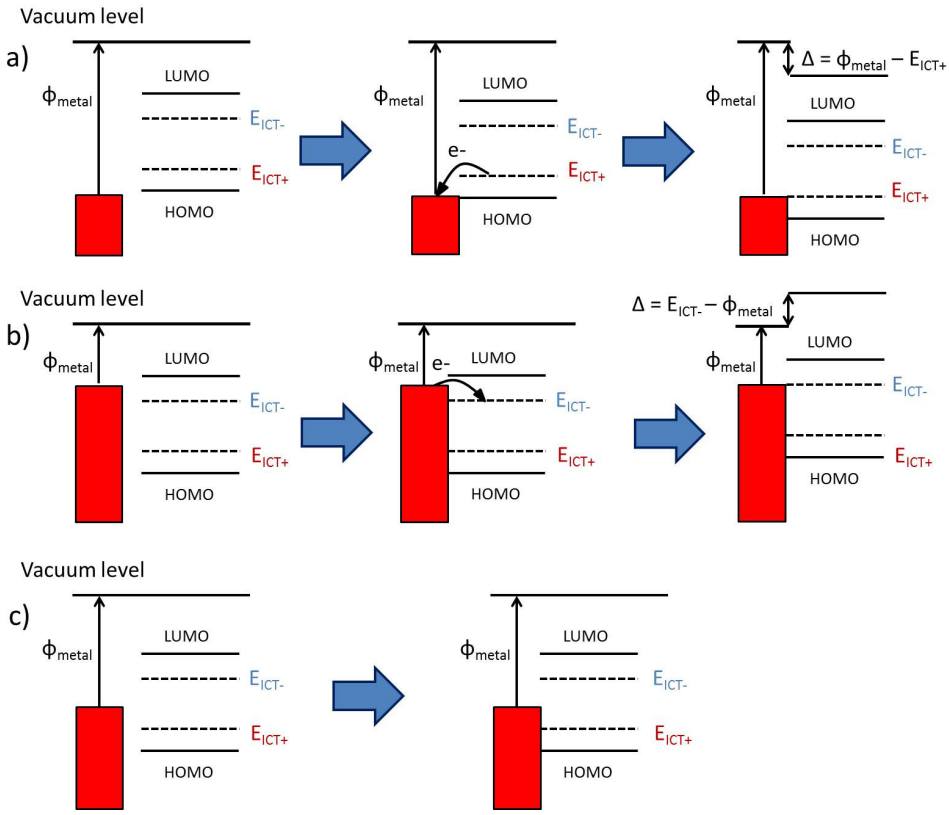

Figure 2.1.1 Schematic of the Fermi level pinning process according to the ICT-model [5]. Note that the energy levels are defined as positive here.

Hence, according to the ICT model, in order to have Ohmic injection the substrate work function should be chosen to be larger than the E_{ICT+} state for hole injection and smaller than the E_{ICT-} state for electron injection. However, as noted by Braun et al, the integer charge transfer states include both electronic and geometrical relaxations as well as screening from the substrate, hence molecules in the bulk are situated in a potentially very different environment than molecules close the interface [5].

2.1.3. Organic-organic interfaces

Interfacial dipole formation does not only occur at organic/metal interfaces, several groups have reported large vacuum level shifts also at organic/organic interfaces [5, 27-29]. In particular it has been shown that the E_{ICT-} state of [6,6]-phenyl-C_{61}-butyric acid methyl ester (PCBM) lies below the E_{ICT+} state of Poly(3-hexylthiophene) (P3HT) resulting in spontaneous charge transfer in P3HT:PCBM bulk heterojunction blends [29]. The interfacial dipole was hypothesized to screen

electrons on the acceptor phase from holes on the donor phase thus reducing recombination [30]. This was suggested as a possible reason to the reduced recombination seen in P3HT:PCBM blends. However, Bao et al suggested that the ICT-states effectively act as trap sites at the donor-acceptor interfaces effectively acting as recombination sites. If this is the case then a large interfacial dipole will significantly increase the rate of trap assisted recombination which in turn increases the overall non-geminate recombination in the blend [31]. It was concluded that BHJ materials should be designed so that no spontaneous charge transfer across the interface occurs.

2.1.4. Interface control and engineering

The large impact of the interfacial properties on the operation of organic electronic devices provides a possibility to improve the performance by introducing thin interfacial layers. In particular self-assembled monolayers (SAMs) can be utilized to modify the work function of metal contacts and control the morphology of subsequently applied layers [32, 33]. It has been shown that the turn on voltages of organic transistors can be efficiently controlled with the introduction of SAMs between the gate dielectric and semiconductor layer due to the vacuum level shift caused by the dipole moment of the SAM [34]. It has also been shown that SAMs can greatly reduce gate leakage as well as increase injection currents [35, 36]. SAMs have also been utilized in organic solar cells with significantly improved efficiencies as a result [37, 38]. Song et al used an ultrathin 3-aminopropyltriethoxysilane monolayer to shift the work function of the cathode in inverted organic solar cells from 4.9 eV to 4.4 eV resulting in an increase in the power conversion efficiency from 0.64% to 4.83% [37].

The underlying mechanisms of the improved device performances are not fully clarified. It has been shown that the turn on voltage shifts observed when using SAMs in transistors is purely due to the vacuum level shift caused by the dipole moment of the SAM. However, it has also been shown that the turn on voltage shifts using SAMs with very different dipole moments do not scale with the intrinsic dipole moments of the SAMs [35]. Since SAMs usually affect both the morphology and the effective work functions the effects are not easy to decouple. Furthermore, the preferred model system for studying these effects is usually thin film transistors, which further complicate the matter since transistors are three terminal systems.

Monti pointed out that the intrinsic (molecular) dipole moment of a SAM is not necessarily a very good measure of the total dipole moment of the layer due to depolarization and screening effects [39]. Hence it is fully possible that the effects observed are purely due to electrostatics but that depolarization and screening

effects has to be taken into account when determining the dipole moment of a molecular layer.

2.2. Recombination

When a photon is absorbed in an organic photovoltaic material an exciton with a high binding energy is formed, as discussed earlier. The (charge neutral) exciton can then diffuse to a donor:acceptor interface where the electron will go to the acceptor LUMO level and the hole will remain on the donor HOMO level. However, due to the high Coulomb binding energy the electron and hole are still bound in a so called polaron pair. The process whereby the polaron pair is split into free charges in a pure material is generally of Onsager-Braun type [40, 41]. In a BHJ the energy difference between the donor and acceptor LUMO levels results in efficient polaron pair splitting. Polaron pairs that do not split up will recombine geminately; geminate recombination is the reunion of charge particles originating from the same molecule [42]. Geminate recombination is a monomolecular process since the recombination rate is directly proportional to the density of polaron pairs [8]. Separated polarons can be extracted at the electrodes, however, disordered organic materials typically exhibit low dielectric constants and charge carrier mobilities leading to high charge carrier densities which in turn results in a high probability of non-geminate recombination. Non-geminate recombination is the reunion of charged species originating from different generation events (photons) and is one of the most important loss mechanisms in organic solar cells [42, 8]. A schematic of the generation and typical recombination processes in BHJ solar cells is given in Figure 2.2.1.

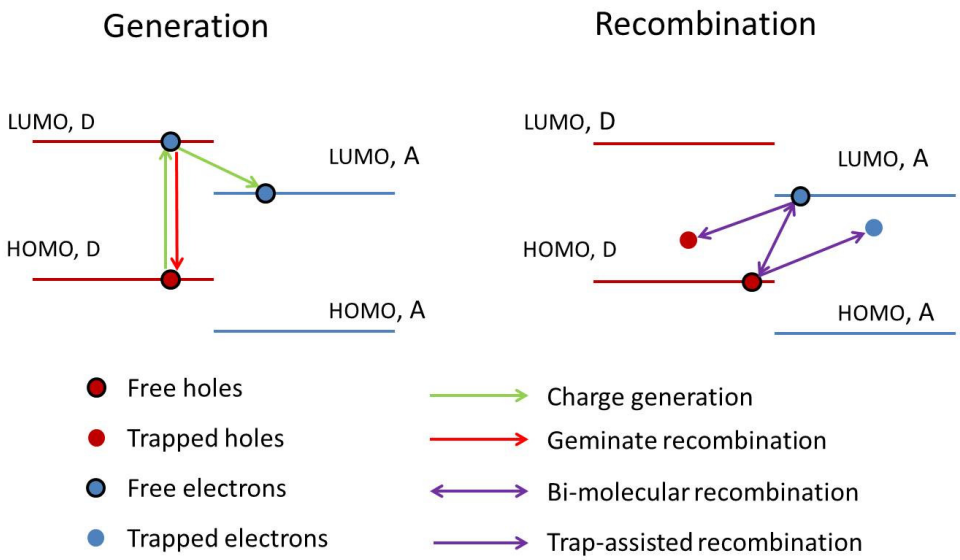

Figure 2.2.1 Schematic of charge generation and recombination processes in BHJ solar cells. HOMO, D(A) and LUMO, D(A) are the HOMO and LUMO levels of the donor and acceptor, respectively.

Non-geminate recombination can be of different types with different reaction orders, for example; mono-molecular recombination (first order), bi-molecular recombination (second order) or tri-molecular recombination (third order). The rate equation for photo-generated charges with non-geminate recombination of order α is given by:

$$\frac{dn}{dt} = G - R = G - rn^{\alpha} \qquad (2.2.1)$$

where n = density of charge carriers, t = time, G = charge generation, R = charge recombination and r = the recombination coefficient. By integrating and solving for $n(t)$ one finds that $n(t) \propto t^{\frac{-1}{(\alpha-1)}}$ at long times for $\alpha > 1$ (for $\alpha = 1$ the decay is exponential). Hence one may distinguish between different recombination mechanisms by observing the decay of photo-generated charge using transient spectroscopy.

2.2.1. Langevin recombination

In organic BHJ the dominant non-geminate recombination mechanism is usually direct (band-to-band) bi-molecular recombination, which is a second order process ($\alpha = 2$). Bi-molecular recombination in these systems is typically observed to be of Langevin type due to the fact that the mean free path (hopping

distance) of the charge carriers is much smaller than the Coulomb capture radius [43, 44]. In 1903 M. P. Langevin developed a theory to describe the rate at which anions and cations recombine in an ion gas. The rate depends only on the velocity at which the ions diffuse towards each other in their mutual Coulomb field, assuming that ion bond formation is instantaneous once the ions are close enough to each other [43]. Langevin recombination is the time reversed process to Onsager-Braun type generation and the Langevin recombination coefficient β_L is given by:

$$\beta_L = q\frac{\mu_{n+}\mu_p}{\varepsilon\varepsilon_0} \qquad (2.2.2)$$

where ε = relative permittivity and ε_0 = the vacuum permittivity. It has been shown by several groups that the recombination rate in certain BHJ blends is much lower than what is expected from Langevin theory [45-47]. The underlying mechanism is heavily debated on and a consensus has not yet been reached.

Deibel et al have suggested that in OPV devices electrons are mostly located close to the cathode where there are no holes and correspondingly the holes are located close to the anode where there are no electrons. Thus recombination can only take place in the middle of the bulk and will involve only a small part of the total number of charges [48]. However, in the case of the BHJ blend P3HT:PCBM double injection measurements also show a reduction in the recombination rate on the order of 10^3 even though in double injection charges are injected at the contacts and driven through the whole bulk to the other contact [49]. Koster et al showed that it is not the faster charge carrier mobility that determines the recombination rate but the slower charge carrier [50]. This means that only the lower mobility should be used in Eq. 2.2.2. However, it was shown by Groves et al that this could only lead to a maximum reduction factor of 10 [51]. Koster et al noted in another paper that the exciton created when an electron and a hole meet in coordinate space (charge encounter complex) can be re-split into a free electron and hole with a certain probability according to Onsager-Braun theory [52]. Murthy et al noted that for several BHJ systems exhibiting reduced recombination the reduction in the recombination seem to be related to the crystallinity of the blend – more crystalline blends tend to have a larger reduction in the recombination rate. They argue that the reason for this is that the charge encounter complex is energetically close or equivalent to the charge transfer state which results in a high probability of exciton re-splitting [47].

Shuttle et al showed using transient photo-induced absorption that the carrier decay dynamics in P3HT:PCBM follows approximately a third order dependence on charge density ($\alpha = 3$), they suggested that r is in fact carrier density dependent

[53]. However, $\alpha = 3$ implies that the recombination is in fact tri-molecular, which has also been suggested to occur in these systems [54].

2.2.2. Shockley-Read-Hall recombination

Recently, several groups have shown that the *JV* characteristics in light and in dark as well as the transient photo-voltage response cannot be explained in terms of Langevin recombination [55-57]. It has been suggested that recombination mainly occurs between trapped and free charges and that the contribution from free to free charge carrier recombination is negligible due to the fact that the majority of charge carriers are trapped. Trap-assisted, or, Shockley-Read-Hall (SRH) type recombination occurs between a trapped and a free charge. In this case the mobility of the trapped charge is zero hence the recombination coefficient is dependent only on the mobility of the free charge. Consider free holes recombining with trapped electrons (n_t), then $R = C_{p,L} n_t p$ where the capture coefficient $C_{p,L}$ is given by [44, 55]:

$$C_{p,L} = e\frac{\mu_n}{\varepsilon\varepsilon_0} \qquad (2.2.3)$$

in accordance with Langevin theory. However, Kirchartz et al noted that using the capture coefficient from Eq. 2.2.3 in drift-diffusion simulations results in a too pessimistic V_{OC}, in order to reproduce experimental data reduced capture coefficients (compared to Equation 2.2.3) have to be assumed [55]. It has been demonstrated that in the case of SRH recombination the reaction order is dependent on the characteristic trap energy E_{Ch} and is different for trapped and free charges [56]. Assuming that the density of trapped and free electrons (n_t and n_f) is equal to the density of trapped and free holes the recombination rate can be expressed in terms of both n_t and n_f as [56]:

$$R \propto n_f n_t = n_t^{\left(\frac{E_{Ch}}{kT}+1\right)} = n_f^{\left(\frac{kT}{E_{Ch}}+1\right)} \qquad (2.2.4)$$

where k is the Boltzmann constant and T is temperature. Hence the reaction order of trapped charge ($\alpha = (E_{ch}/kT + 1)$) increases for increasing trap depth whereas it decreases for free charges ($\alpha = (kT/E_{ch} + 1)$). Thus if free charges are observed the recombination will be practically monomolecular for large E_{Ch}.

2.2.3. Effect of anisotropic transport

Some polymers, like P3HT, order themselves into a crystalline lamellar structure. G. Juška and others have suggested that in these systems the charge transport is mainly restricted to two dimensions since the mobility in the lamellar plane is significantly larger than the out of plane mobility [58-60]. In this case the

hole is delocalized over the polymer lamella whereas the electrons are more localized, as illustrated in Figure 2.2.2.

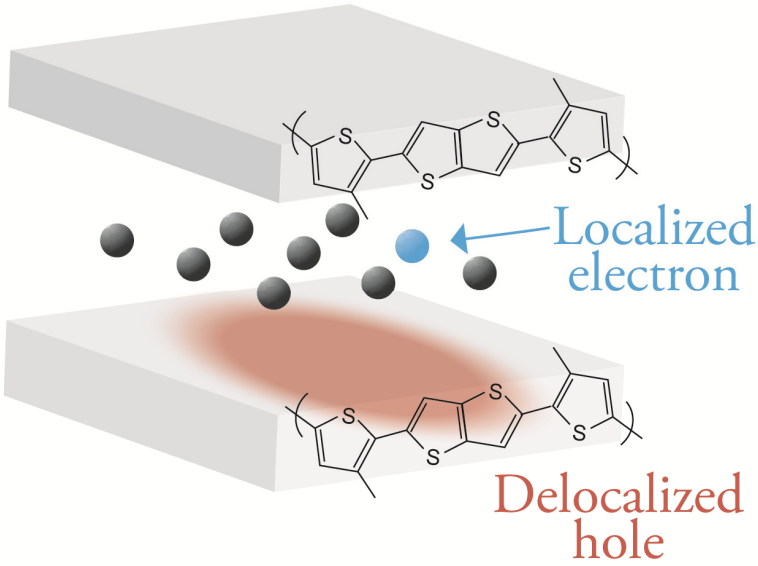

Figure 2.2.2 Schematic of a delocalized hole in a lamellar system [Paper V].

This fact suggests that in the case of crystalline blends the standard three dimensional Langevin formalism should be replaced by a two dimensional one (2D-Langevin). The decay of light generated charge carriers is then given by [58, Paper V]):

$$\frac{dp}{dt} = G - \beta_{2D} np = G - \gamma_{2D}(np)^{5/4} \qquad (2.2.5)$$

where $\beta_{2D} = \gamma_{2D}(np)^{1/4}$ and $\gamma_{2D} = \frac{3\sqrt{\pi}}{4} l^{3/2} \beta_L$ is the two dimensional Langevin recombination coefficient and l = the lamellar spacing. Assuming $n \approx p$ gives:

$$\frac{dp}{dt} = G - \gamma_{2D} p^{5/2} \qquad (2.2.6)$$

and solving for p yields:

$$p(t) = \left(\frac{1}{p_0^{-3/2} + \frac{3}{2}\gamma_{2D} t} \right)^{2/3} \qquad (2.2.7)$$

which is $\propto t^{-2/3}$ at long times. The apparent reduction in the recombination coefficient versus 3D-Langevin ($r = \beta_L$) will be given by [58]:

$$\frac{\beta_{2D}}{\beta_L} = \frac{3\sqrt{\pi}}{4} l^{3/2} p^{1/2} \tag{2.2.8}$$

Calculated values for P3HT:PCBM are in excellent agreement with measurements [58].

The above results are valid for free charges. If the majority of electrons are trapped a similar derivation for the capture coefficient $C_{p,2D}$ between free holes and trapped electrons gives [Paper V]:

$$C_{p,2D} = \frac{3\sqrt{\pi}}{4} \left(l^3 \sqrt{n_t p}\right)^{1/2} C_{p,L} \tag{2.2.9}$$

where $C_{p,L}$ is given by Equation 2.2.3. If the amount of trapped electrons is much larger than the amount of free electrons and holes trap-assisted recombination between free holes and trapped electrons become dominating, the recombination term of Equation 2.2.1 is consequently given by [Paper V]:

$$R = C_{p,2D} n_t p = \gamma_{2D} \left(\frac{\mu_p}{\mu_p + \mu_n}\right) (n_t p)^{\frac{5}{4}} \propto p^{5/4} \tag{2.2.10}$$

CELIV, time-of-flight (ToF), double injection and transient absorption measurements on P3HT:PCBM have been reported to be in agreement with the 2D-Langevin model [58]. However, steady-state measurements such as the diode ideality factor and the light ideality factor on the same material blend show mainly SRH type behavior. There appears to be a discrepancy between transient and steady-state measurements. Furthermore, Gorenflot et al showed using transient photo induced absorption that the recombination in pure P3HT is perfectly consistent with ordinary 3D-Langevin recombination despite the fact that pure P3HT is also a lamellar system [61]. Here there is another discrepancy since ToF and photo-CELIV measurements on pure P3HT are consistent with 2D-Langevin [62, 63].

3. Experimental

3.1. Materials

This thesis presents studies performed on a multitude of different materials such as polymers, organic small molecules and a fullerene derivative. The active materials are briefly presented below. A schematic of the materials used is shown in Figure 3.1.

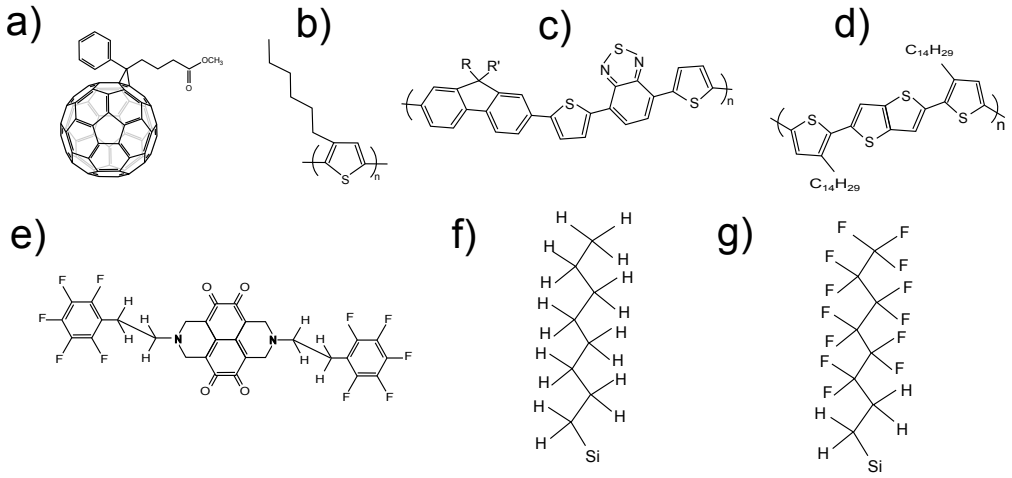

Figure 3.1 Schematic of the molecules used a) PCBM b) P3HT c) APFO3 d) PBTTT e) 5FPE-NTCDI f) OTS and g) FOTS. Images a) - c) are courtesy of H. Aarnio.

Bulk heterojunction materials

Various fullerene derivatives are the most common acceptor materials in BHJ solar cells, and [6,6]-phenyl-C_{61}-butyric acid methyl ester (PCBM) together with [6,6]-phenyl-C_{71}-butyric acid methyl ester are arguably the most used [64]. PCBM as first synthesized by Hummelen et al and has been widely used since the invention of the bulk heterojunction by Yu et al in 1995 [10, 65]. However, recently other fullerene derivatives are becoming increasingly more popular due to the limited light absorption of PCBM [64].

Poly(3-hexylthiophene) (P3HT) forms a crystalline lamellar structure separated by an amorphous inter-lamellar region [66]. P3HT blended with the fullerene derivative PCBM is the most studied BHJ blend to date showing a PCE up to and above 5 % [67]. P3HT and PCBM blended in a BHJ form phase-separated

crystalline domains roughly 10 nm in size [11]. Furthermore, it has been shown that the pure polymer and fullerene domains are surrounded by a composite domain containing both polymer and fullerene [68]. The recombination dynamics in P3HT:PCBM is highly debated and the morphology of the blend adds complexity to the problem [55, 60, 69].

APFO3 is one in a class of alternating polyfluorene copolymers [70]. The copolymers consist of various electron withdrawing and electron donating groups in a donor-acceptor-donor structure. This structure provides the opportunity of shifting the HOMO and LUMO levels in order to optimize the absorption [71]. Geminate recombination has been shown to be the dominating recombination mechanism at moderate light intensities [71]. The main advantage of APFO3:PCBM solar cells is the high V_{OC} of around 1V.

Poly[2,5-bis(3-tetradecylthiophen-2-yl)thieno[3,2-b]thiophene] (PBTTT) is a polymer that in the solid state exhibits exceptionally high degree of order due to interdigitation of side-chains between adjacent lamellae [72]. When blended with PCBM in a 1:1 weight ratio all the PCBM molecules will intercalate between the side chains of the polymer forming a bi-molecular crystal with approximately one fullerene molecule per monomer [72, 73]. In a 1:1 weight ratio electron transport is limited by the long inter-site distances, at higher fullerene loadings pure PCBM domains are formed between the polymer lamellae greatly increasing the electron mobility [74, 75].

Small organic molecules

N,N′-bis(2-(pentafluorophenyl)ethyl)-1,4,5,8-naphthalenetetracarboxylic acid diimide (5FPE-NTCDI) is one in a class of many small molecule organic semiconductors synthesized by Katz and others [76, 77]. The NTCDIs are used in n-channel transistors exhibiting good operational stability in air and high mobility, approaching 1 cm^2/Vs [77]. Furthermore, 5FPE-NTCDI has been used in transparent OFETs showing excellent performance [76].

The SAMs triethoxy(octyl)silane (OTS) and 1H,1H,2H,2H-perfluorooctyltriethoxysilane (FOTS) have been used to modify interfacial properties such as increase surface conductivity [78] and reduce gate leakage [35]. The molecules will self-assemble on aluminum oxide and they can be easily grown in a vacuum oven. FOTS has a much larger intrinsic dipole moment than OTS due to its fluorinated tail [79].

Metal oxide

Aluminum has been used extensively as a cathode contact due to its low work function. However, the low work function also makes aluminum highly susceptible

to oxidation, a thin layer of aluminum oxide (AlO_x) is formed on top of any aluminum surface when in contact with oxygen. AlO_x is an insulator which means that oxide formation at the cathode-active layer interface essentially forms a blocking layer which has a detrimental effect on the device performance [80].

AlO_x can also be used in beneficial ways, due to its rather high relative dielectric constant ($\varepsilon \approx 9.5$) and its compatibility with flexible substrates it has been used as dielectric in thin film transistors. However, several reports show a high density of defects and traps in AlO_x leading to trap-assisted conduction and gate leakage [81, 82].

3.2. Charge extraction by a linearly increasing voltage

The CELIV method was first demonstrated by Juška et al on microcrystalline silicon [83] and later on conjugated polymers [84]. The method was later expanded to the case with light generation of charges (photo-CELIV) [85, 86]. It has since then become one of the most common methods to measure the mobility in low-conductivity materials, mainly organic semiconductors. The main advantage of CELIV is that it allows one to measure both the amount of extracted charge carriers and the (fully relaxed) mobility as a function of time. Lately several additional expansions have been demonstrated such as the metal-insulator-semiconductor CELIV (MIS-CELIV) and the injected charge CELIV (i-CELIV), where charges injected using an offset voltage are probed, and the doping-induced capacitive mode CELIV (doping-CELIV), where the depletion region capacitance is probed [87-89]. However, this chapter will focus solely on CELIV in the dark (coined dark-CELIV for clarity) and photo-CELIV.

3.2.1. Dark-CELIV

A schematic of the dark-CELIV method is shown in Figure 3.2.1. A linearly increasing voltage is applied over a sandwich configuration device (at flat band conditions) with at least one blocking contact (or revers bias in a diode configuration). The corresponding current transient consists of a time independent (capacitive) response ($j(0)$) and a time dependent response (Δj) due to extraction of equilibrium charges in the film. If $j(0)$ is not clearly visible due to high density of extracted charge another pulse can be applied after a delay time t_{del}. Furthermore, by varying t_{del} the regeneration of charges in the devices can be probed. If the contacts are asymmetrical the built-in field needs to be cancelled out by applying an offset voltage U_{OFF}.

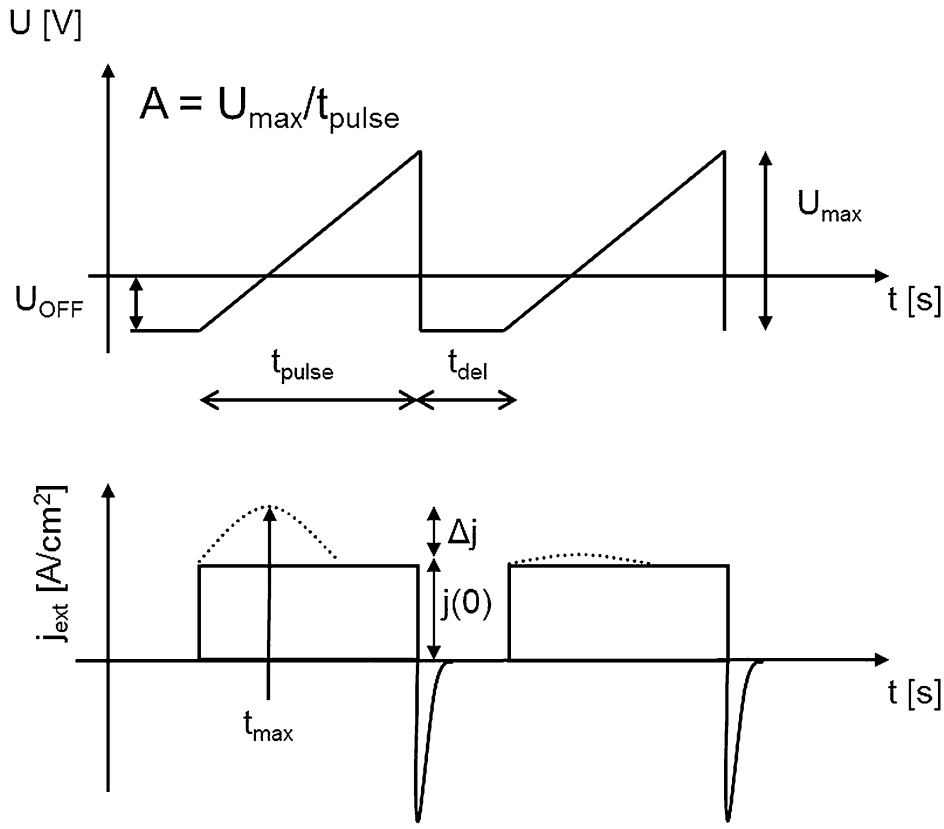

Figure 3.2.1 Schematic of the dark-CELIV technique.

From the time the current transient reaches its maximum value (t_{max}) the mobility μ can be calculated as [90]:

$$\mu = K\frac{d^2}{At_{max}^2} \qquad \text{when } \Delta j << j(0) \qquad (3.2.1)$$

$$\mu = \frac{j(0)d^2}{\Delta j A t_{max}^2} \qquad \text{when } \Delta j >> j(0) \qquad (3.2.2)$$

where K = 2 for surface generation and 2/3 for volume generation, d = thickness and A = the voltage rise speed. In most cases however, $\Delta j \sim j(0)$ and then the mobility will approximately be given by:

$$\mu = K\frac{d^2}{At_{max}^2\left(1+0.36\frac{\Delta j}{j(0)}\right)} \qquad (3.2.3)$$

The factor 0.36 in the denominator is empirically derived. Furthermore, from the initial rise of the charge extraction transient (*j(0)*) one can calculate the sample capacitance *C* as [91]:

$$C = \frac{j(0)S}{A} \tag{3.2.4}$$

where *S* is the contact area. If the dielectric constant is also known the thickness *d* of the dielectric can be calculated as:

$$d = \frac{A\varepsilon\varepsilon_0}{j(0)} \tag{3.2.5}$$

By integrating Δj over t_{pulse} the density of the extracted charge n_{ext} can be obtained as:

$$n_{ext} = \frac{1}{ed}\int_0^{t_{pulse}} \Delta j(t)dt \tag{3.2.6}$$

where *e* is the elementary charge.

3.2.2. Photo-CELIV

Figure 3.2.2 shows a schematic of the photo-CELIV technique. In photo-CELIV charges are generated with a light pulse, the voltage pulse is applied after a variable delay time t_{del}. When using photo-CELIV it is critical to set a proper offset voltage in order to cancel out the built-in field, not only will the calculated mobilities not be correct (Juška assumes zero built-in voltage in his original analysis) but if there is a considerable potential drop over the device during photo-generation charges will be extracted to the outer circuit before the voltage pulse can be applied. The offset voltage should be chosen so that as little charge as possible is extracted to the outer circuit prior to applying the voltage pulse while keeping the charge injection from the contacts due to the applied voltage as little as possible. In thin films especially this is non-trivial since the electric field in the device will be position and time-dependent. Provided that the proper offset can be applied with little or no charge injection equations 3.2.1-3.2.3 are valid.

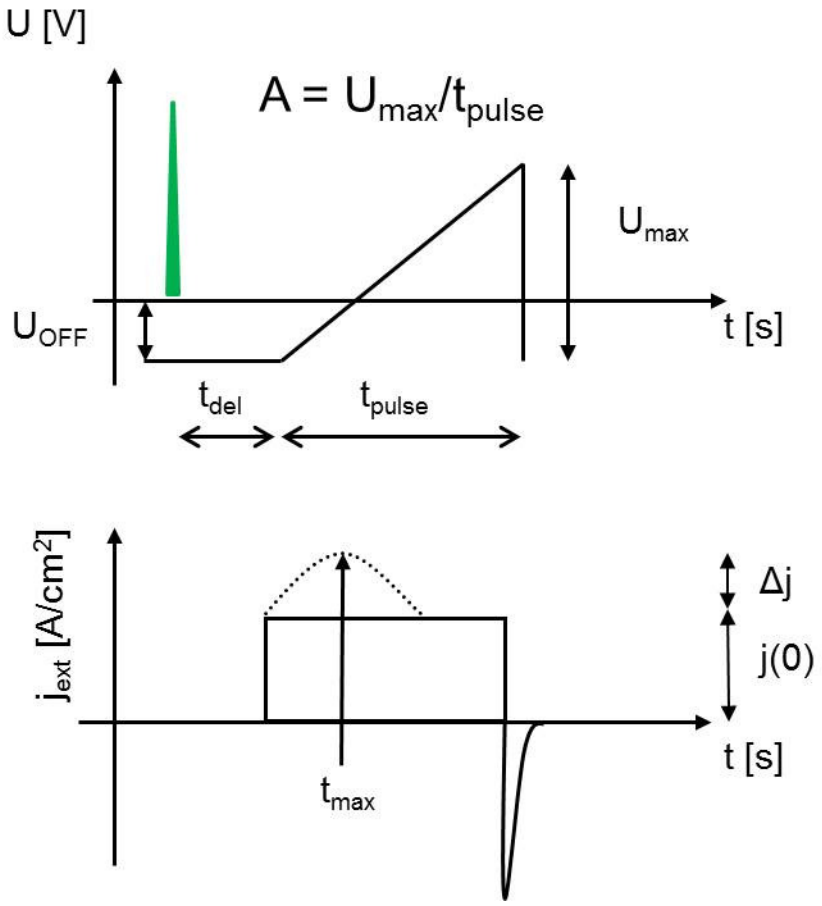

Figure 3.2.2 Schematic of the photo-CELIV technique.

Equation 3.2.3 has been debated to some extent in the literature and some slight alterations have been proposed [92]. However, it was shown by Juška et al (in the case of Langevin recombination) that in order to calculate the mobility correctly the generation profile needs to be fully taken into account [93]. For optically thick films or high excitation intensities the error in the mobility calculated using Equation 3.2.3 can be over an order of magnitude. However, for optically thin films with low or moderate excitation intensities the errors are small. A similar procedure for calculating the mobilities in the case of reduced Langevin recombination has not yet been published.

3.3. Photoinduced absorption

When photo-excitations are created in a material the absorbance of the material will change, the difference in absorbance is called photo-induced absorption (PA). This is due to the fact that the photo-excitations absorb light at different characteristic energies than the material in the ground state. Hence when the material is excited the linear absorption will decrease and new absorption bands will appear. The change in the transmission, ΔT, is thus directly correlated with the photo-excitations. This allows for a possibility to observe the photo-excitation dynamics in a pump probe type of setup where one beam is used for photo-generation (pump) and the other is used to detect differences in the transmission (probe). There are two different types of PA measurements; continous wave (cw-PA) and transient (t-PA).

In cw-PA the sample is excited using a pump light which is modulated using a mechanical chopper with frequency ω. The probe light is continuously on and ΔT is detected using a lock-in amplifier, a monochromator is used to separate out single wavelengths of the white light probe. ΔT then needs to be corrected for photo-induced luminescence and scattered probe light which is measured by performing the same measurement with the probe off. Conversely by keeping the probe on and the pump off the transmission T is obtained. The photo-induced absorption is then given by $-\Delta T/T$. The density of the photo-excitations can be estimated as $n=(-\Delta T/T)/(d\sigma)$ where d is the thickness and $\sigma = 10^{16}$ cm^2 is the absorption cross section [94]. ΔT is detected both in-phase with the mechanical chopper and out-of-phase, i.e. the quadrature; the total PA(ω) is then given by [95]:

$$PA(\omega) = PA_I(\omega) - iPA_Q(\omega) \tag{3.3.1}$$

where $PA_I(\omega)$ is the in-phase PA and $PA_Q(\omega)$ is the quadrature PA. Another way of representing the signal is in polar coordinates as a function of the radius (PA_R) and the phase (φ) [95]:

$$PA(\omega) = PA_R(\omega)e^{i\varphi(\omega)} \tag{3.3.2}$$

where $PA_R(\omega) = \sqrt{PA_I(\omega)^2 + PA_Q(\omega)^2}$ and $\varphi(\omega) = \arctan(\frac{PA_Q(\omega)}{PA_I(\omega)})$. Assuming non-dispersive excitations the effective excitation lifetime τ_0 is given by [95]:

$$\tau_0 = \frac{\tan(-\varphi)}{\omega} \tag{3.3.3}$$

3.4. Light ideality factor

By observing the decay of photo-generated charges using transient spectroscopy measurements it is in some cases possible to determine the dominating recombination mechanism. However, in transient spectroscopy charges are typically generated in a mostly empty DOS, which is not necessarily representative of operating conditions. Complementary steady-state techniques are needed; the light ideality factor offers such a possibility [96, 97].

It has been shown (empirically) that the V_{OC} scales with the light intensity (I) as follows (assuming Ohmic contacts) [96, 97]:

$$eV_{OC} \propto mkT \ln(I) \tag{3.4.1}$$

where m is the so called light ideality factor. At open-circuit conditions all photo-generated charges recombine (since the current is zero) and we have $G = R$, insertion into Equation 2.2.1 yields:

$$G = rn^{\alpha} \tag{3.4.2}$$

Assuming that the majority of the carriers are photo-generated we set $n \approx p$.
By using $p = n$ in Equations 1.3.2 and 3.42, and solving Equation 3.4.2 for p one finds

$$eV_{OC} = E_g^{DA} - \frac{2}{\alpha} kT \ln\left(\frac{r(N_c N_v)^{\alpha/2}}{G}\right) \propto \frac{2}{\alpha} kT \ln(I) \tag{3.4.3}$$

since $G \propto I$. The corresponding light ideality factor is then given by $m = \frac{2}{\alpha}$. Hence a system showing ordinary Langevin recombination will have m = 1 whereas a system governed by 2D-Langevin will have m = 0.8.

In the case of SRH recombination the light ideality factor is dependent on E_{Ch} according to [55]:

$$m = \begin{cases} \left(\frac{1}{2} + \frac{kT}{2E_{Ch}}\right)^{-1} & \text{for} \quad E_{Ch} > kT \\ 1 & \text{for} \quad E_{Ch} \to 0 \end{cases} \tag{3.4.4}$$

Hence the ideality factor will range between 1 and 2, provided that the capture coefficients are given by Equation 2.2.3 (i.e. in accordance with Langevin theory). If, however, the transport is 2D-limited the capture coefficient is instead given by Equation 2.2.9 the recombination is proportional to $p^{5/4}$ which leads to an ideality

factor of 1.6. Thus a 2D-Langevin system is expected to have a light ideality factor between 0.8 and 1.6 with a larger m indicating deeper lying and/or more traps.

When determining the light ideality factor it is important to make sure that the light intensity is not too high; when the light intensity is high enough the V_{OC} will saturate to the V_{bi}. This is caused by an increased surface recombination due to the lack of driving force for extraction [98]. Also the contacts should be non-blocking since the V_{OC} is affected by injection and extraction barriers according to Equation 1.4.1 [99, Paper IV].

3.5. Drift-diffusion simulations

Drift-diffusion simulations have proven to be very useful for understanding the device physics of BHJ solar cells, in particular the effects of contacts, charge transport and recombination [18, 19, 52, 100]. The device is assumed to consist of an effective semiconductor with $E_{LUMO} = E_{LUMO,A}$ and $E_{HOMO} = E_{HOMO,D}$ sandwiched between two contacts with work functions Φ_{an} (anode) and Φ_{cat} (cathode). The equations to be solved are the Poisson equation and the continuity equation for electrons and holes [101]. The Poisson equation relates the space charge to the electric field F:

$$\frac{dF}{dx} = -\frac{q}{\varepsilon\varepsilon_0}(n - p + N_n - N_p + n_t - p_t) \tag{3.5.1}$$

where $N_{n(p)}$ is the density of n (p) dopants and n_t (p_t) is the density of trapped electrons (holes). The continuity equation for electrons and holes is given by:

$$\frac{1}{q}\frac{dJ_n}{dx} + G - R = 0 \tag{3.5.2}$$

$$-\frac{1}{q}\frac{dJ_p}{dx} + G - R = 0 \tag{3.5.3}$$

where the current densities for electron and holes are given by:

$$J_n = q\mu_n nF + \mu_n kT\frac{dn}{dx} \tag{3.5.4}$$

$$J_p = q\mu_p pF - \mu_p kT\frac{dp}{dx} \tag{3.5.5}$$

The equations are solved numerically following an approach developed by Scharfetter and Gummel [101-103]. The charge injection and extraction at the electrodes is modelled using an effective surface recombination; the electron current at the cathode is given by:

$$J_n(d) = -qS_{n,cat}(n(d) - n_{cat})) \qquad (3.5.6)$$

where $S_{n,cat}$ is the surface recombination velocity for electrons at the cathode, n_{cat} is the cathode electron density at thermal equilibrium and d is the device thickness. A detailed description of the model is given in [Paper IV].

4. Results and discussion

4.1. Metal-organic interfaces – ideal contacts

In paper I the origin of the equilibrium charge reservoir in P3HT:PCBM based devices was clarified. According to the ICT-model, an Ohmic contact implies that the work function of the metal is pinned to the ICT+/ICT- levels of the organic semiconductor [5]. In this case there will be a charge reservoir at the contact, possibly stretching several tens of nanometers into the organic [26], the charge density of the reservoir being determined by the difference between the metal work function and the ICT+/ICT- levels of the organic. This is illustrated in Figure 4.1.1 which shows dark-CELIV current transients of a ITO/PEDOT:PSS/P3HT:PCBM/LiF/Al device at different offset voltages. It can be seen that at short circuit conditions (U_{OFF} = 0 V) there are extractable equilibrium charges in the device. For increasing U_{OFF} (towards open circuit conditions) it can be seen that the amount of charges increases and at U_{OFF} = 0.5 V the increase is very large due to the dark injection current (seen as a negative current at t < 0). Furthermore, it can be noted that the charge reservoir is replenished in the device by diffusion of charges from the contacts, this is seen as a negative current which stretches tens of microseconds after the voltage pulse.

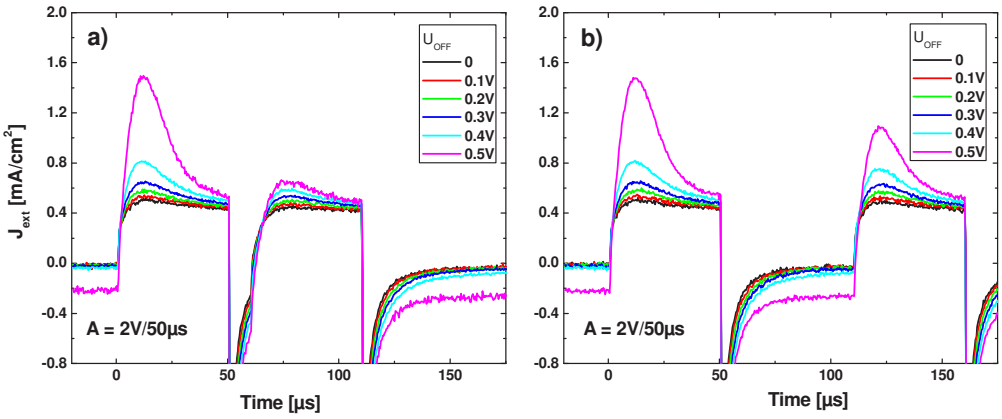

Figure 4.1.1 CELIV transients of a ITO/PEDOT:PSS/P3HT:PCBM/LiF/Al device at different offset voltages.

Figure 4.1.2 shows dark-CELIV current transients of a) an Al/P3HT:PCBM/Al device and b) an ITO/P3HT:PCBM/Au device demonstrating that Fermi level pinning occurs both at the Al/PCBM and Au/P3HT interface. Figure 4.1.2 a) also shows that the amount of dark charges increase rapidly when the PCBM content is increased from 20 % to 40 % which means that a certain amount of PCBM is needed for charge transfer to occur. The size of the reservoir is in the order of 10^{15}-10^{16} cm^{-3}, assuming that the reservoir stretches evenly over the whole device, which is probably not the case. More likely the charge density is >> 10^{16} cm^{-3} in the vicinity of the contact which is much larger than what is expected from pure diffusion from the contacts, providing additional support for the ICT-model. Furthermore, according to Aarnio et al [29], since the ICT- level of PCBM is lower in energy than the ICT+ level of P3HT it is impossible to choose the contact work functions so that vacuum alignment is achieved at both contacts, i.e. there will always be some spontaneous charge transfer. However, by choosing a metal with a work function as close as possible to the ICT+ and ICT- levels the amount of transferred charge can be minimized. Tin has a work function of ~ 4.1 eV (as measured by Kelvin probe) and is a possible candidate.

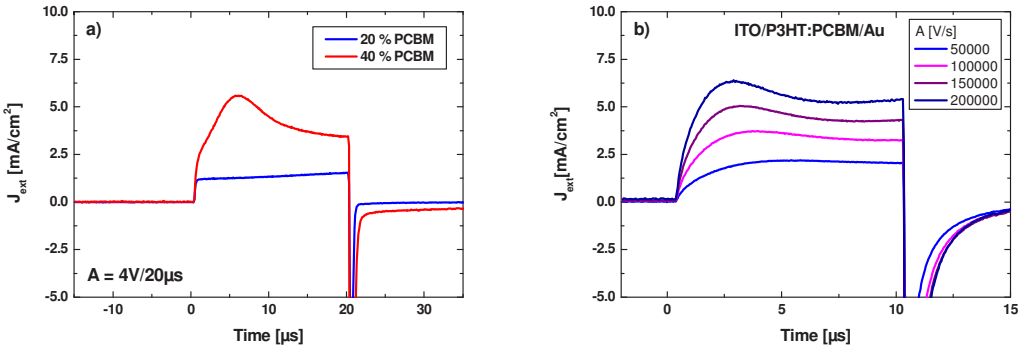

Figure 4.1.2 CELIV transients of a) an Al/P3HT:PCBM/Al device and b) an ITO/P3HT:PCBM/Au device.

Figure 4.1.3 shows dark-CELIV current transients of an ITO/Sn/P3HT:PCBM/Sn/Au device, the device is practically depleted from equilibrium charge in excellent agreement with the ICT-model. Furthermore, the fact that the dark carrier density is so low in the Sn-device indicates that the equilibrium charges cannot be caused by doping of the active layer or spontaneous charge transfer at the P3HT:PCBM interface but are indeed contact related.

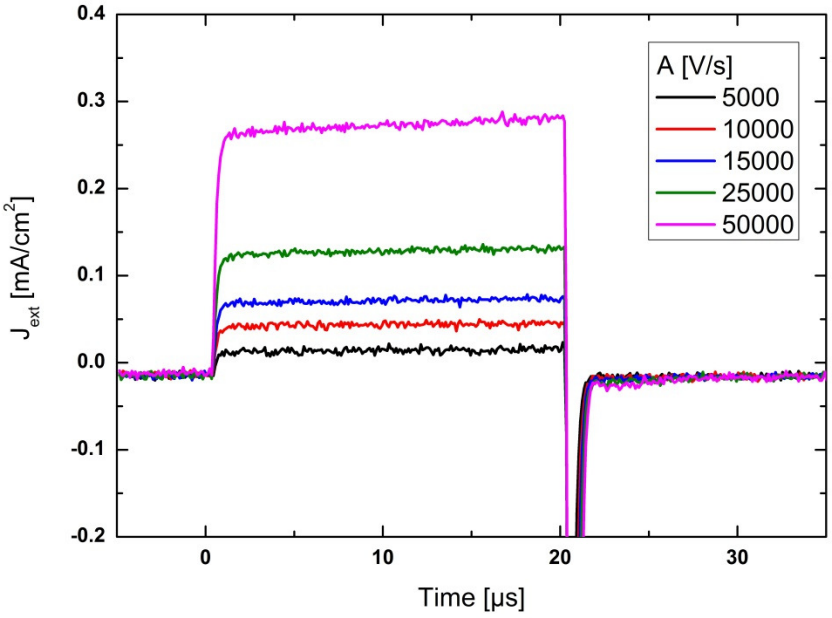

Figure 4.1.3 CELIV transients of an ITO/Sn/P3HT:PCBM/Sn/Au device.

Spontaneous charge transfer at metal-organic interfaces has direct consequences for the operation of organic electronic devices. The interfacial charge reservoir is directly related to a bending of the energy bands according to the Poisson equation; the larger the reservoir the larger the band bending. If the ICT-model holds true, careful interfacial design is essential to avoid losses in performance.

4.2. Metal-organic interfaces - Non-Ideal contacts

Imperfect contacts may arise from several different reasons such as misaligned energy levels with resulting injection barriers, low surface recombination velocities and doping in the vicinity of the contacts. Device performance will be contact limited if these imperfections are severe. Non-ideal contacts are often a result of degradation with a reduced performance as a result. Especially low work function metals are particularly sensitive to degradation by oxidation.

4.2.1. Trapping in aluminum oxide

In paper II the effect of trapping in AlO_x based devices was clarified with the CELIV technique. Trap densities as high as 10^{19} cm^{-3} have been reported in anodic AlO_x dielectrics. Such a large density of trap states will have a significant effect on the extraction current transients. Consider a square shaped trap DOS with a trap density N_t and width ΔE_t as illustrated in Figure 4.2.1.

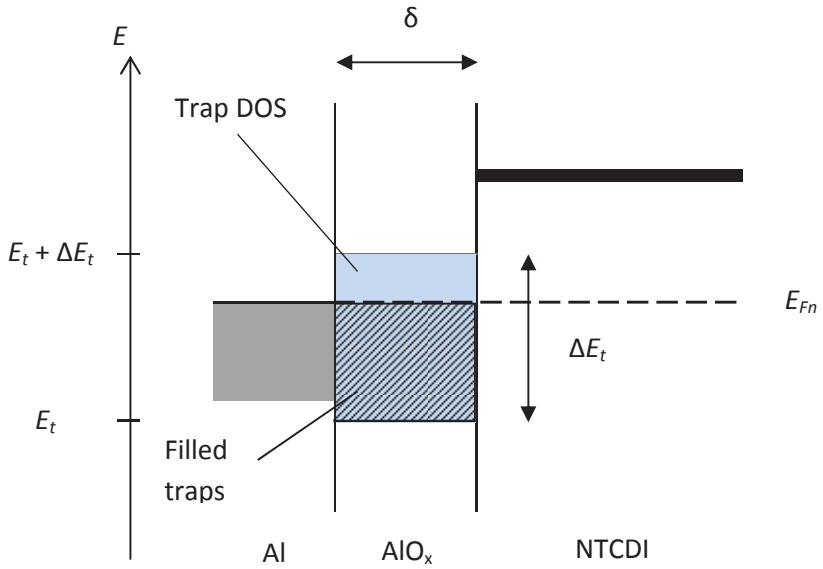

Figure 4.2.1 Schematic of the trap DOS in AlO_x under flatband conditions. E_{Fn} is the quasi Fermi level, E_t is the lowest lying trap level, ΔE_t is the width of the trap distribution and δ is the thickness of the oxide.

When the quasi Fermi level is moved upwards through the DOS, trap sites will be filled and the number of occupied traps n_t is increased. When applying a sufficiently slow linearly increasing voltage pulse over the oxide layer the trap filling will give rise to a displacement current $j_D = j(0) + j_{D,t}$ if the quasi Fermi level is within the trap DOS, where $j(0) = CA$ and

$$j_{D,t} = q\delta\frac{dn_t}{dt} = \frac{q^2\delta N_t A}{\Delta E_t} \qquad (4.2.1)$$

When $E_{Fn} > E_t + \Delta E_t$, $n_t = N_t$, and $j_{D,t} = 0$ and $j_D = j(0)$. In reality a square shaped DOS is unlikely, but the effect will be qualitatively the same.

In order to observe and clarify the trap-filling in AlO_x, diodes consisting of Al/AlO_x as bottom contact and Au as top contact with 5FPE-NTCDI sandwiched in between, was chosen as model system. 5FPE-NTCDI was chosen due to the fact that the HOMO and LUMO levels of 5FPE-NTCDI forms blocking contacts with Au and Al enabling observation of the purely capacitive $j_{D,t}$. Figure 4.2.2 shows the CELIV current transients at different offset voltages for a Al/AlO_x/5FPE-NTCDI/Au device.

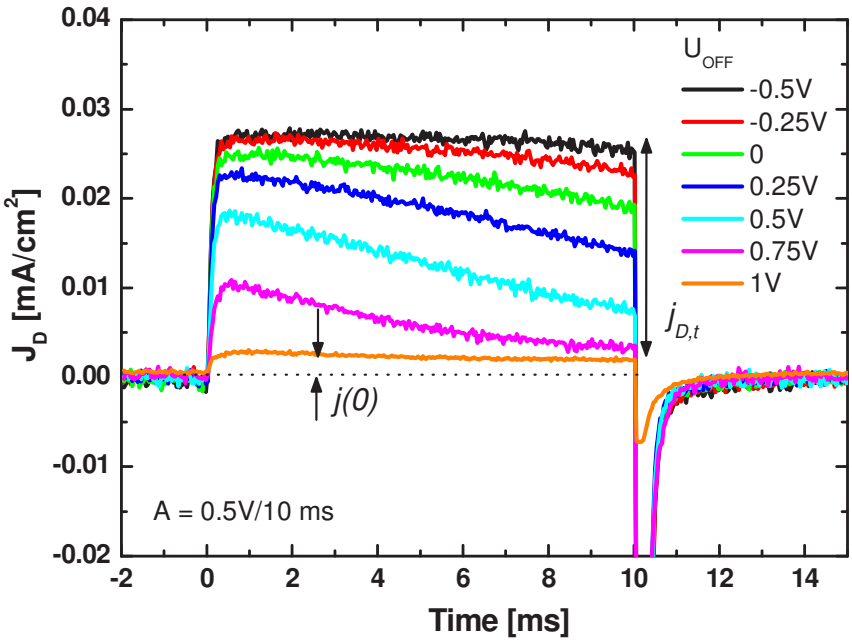

Figure 4.2.2 CELIV current transients at different offset voltages for an Al/AlO_x/5FPE-NTCDI/Au device. The voltages are applied to the Au contact and A = +0.5 V/10ms.

One can see that when a positive offset of 1 V is applied the current transient at t = 10 ms corresponds roughly to the *j(0)* calculated using equation 3.2.5 (*j(0)* = 1.55 μA/cm^2 with d = 100 nm and ε = 3.5). For smaller offset voltages the displacement current increases in magnitude to finally almost saturate at U_{OFF} = -0.5 V. The saturated displacement current is roughly 15 times larger than *j(0)*. By insertion of the values into Equation 4.2.1 the trap density is in the order of 10^{19} cm^{-3}, assuming that ΔE_t = 1 eV and δ = 2 nm.

Due to the high trap density and the blocking contacts all of the potential drop in the device will occur over the oxide layer. Hence the displacement current, and in particular the potentials at which the displacement current saturates is sensitive to the built-in voltage of the device. By introducing a self-assembled monolayer (SAM) between the oxide and the NTCDI the vacuum level will be shifted due to the dipole moment of the SAM thus changing the built-in voltage. By observing at what offset voltages the displacement current saturates one can obtain an estimate of the vacuum level shift, provided that the shape of the trap DOS is not affected by the introduction of the SAM.

Figure 4.2.3 shows the displacement current as a function of applied voltage for a) an Al/AlO_x/5FPE-NTCDI/Au device b) an Al/AlO_x/OTS/5FPE-NTCDI/Au device and c) an Al/AlO_x/FOTS/5FPE-NTCDI/Au device. The voltages are applied to the Au contact and A = +0.5 V/10ms. Since there are no clear kinks where the saturations to the maximum and minimum displacement currents occur (the positions of which could be compared between different devices), the voltage at which the displacement current reaches half of its maximum value can be used as a measure of the vacuum level shift. The shifts as obtained from Figure 4.2.3 are 0.45V and 0.85V towards more negative voltages on the Au-contact for OTS and FOTS respectively. This provides a method of probing the vacuum level shift in operating devices. The shifts observed are slightly smaller than the threshold voltage shifts observed for transistors with p-doped silicon as gate, which were 0.79 V for OTS and 1.83 V for FOTS [35]. However, the vacuum level shift is roughly twice as large for FOTS than with OTS both the in transistors and in the diodes which does not scale with the dipole moments of the individual molecules, since the dipole moment of FOTS is more than ten times larger than the dipole moment for OTS [35].

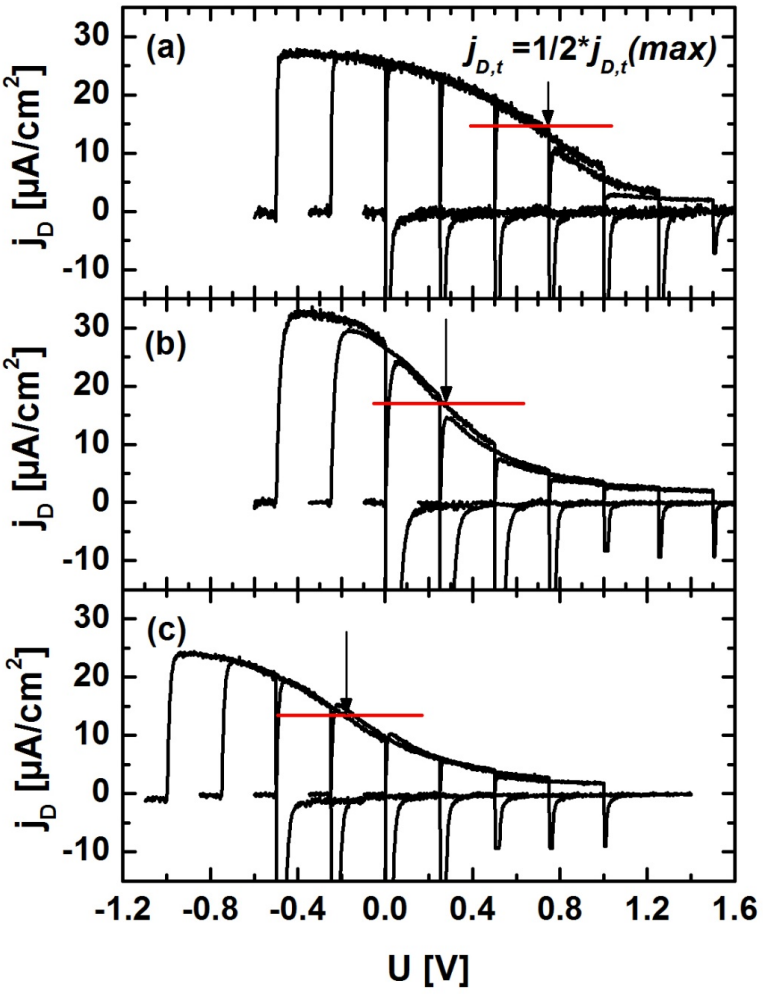

Figure 4.2.3 The displacement current as a function of applied voltage for a) an Al/AlO_x/5FPE-NTCDI/Au device b) an Al/AlO_x/OTS/5FPE-NTCDI/Au device and c) an Al/AlO_x/FOTS/5FPE-NTCDI/Au device. The voltages are applied to the Au contact and A = +0.5 V/10ms.

A trap DOS of this size will severely affect device performance, the space charge of the occupied traps will cause band bending similar to the case of Fermi-level pinning discussed above. In addition, when turning on a transistor with an AlO_x gate dielectric the trap states will be filled as the quasi Fermi level is moved up through the trap DOS which slows down device operation. This effect is not

necessarily limited to AlO_x; similar results were obtained also for thin (~ 10 nm) silicon oxide based devices.

4.2.2. Reduced performance due to degradation

Paper III is an attempt to decouple different degradation mechanisms leading to reduced performance. Figure 4.2.4 a) shows the *JV* curves of a pristine and a degraded ITO/PEDOT:PSS/APFO3:PCBM/LiF/Al device. The pristine device was encapsulated directly after fabrication whereas the degraded device was encapsulated after having been under simulated sunlight in ambient conditions for three days. A clear s-shape can be seen in the *JV* characteristics for the degraded device. The J_{SC} is also lower in the degraded device but the V_{OC} is virtually unchanged. Girtan et al showed that for devices with ITO/PEDOT:PSS as anode the V_{OC} decreases when exposed to ambient conditions which is not seen here, implying that either the active layer or the LiF/Al cathode is the main cause of the degraded performance [104]. The lowered J_{SC} may be, at least partially, attributed to bleaching of the active layer as seen from the absorption spectrum in Figure 4.2.4 b).

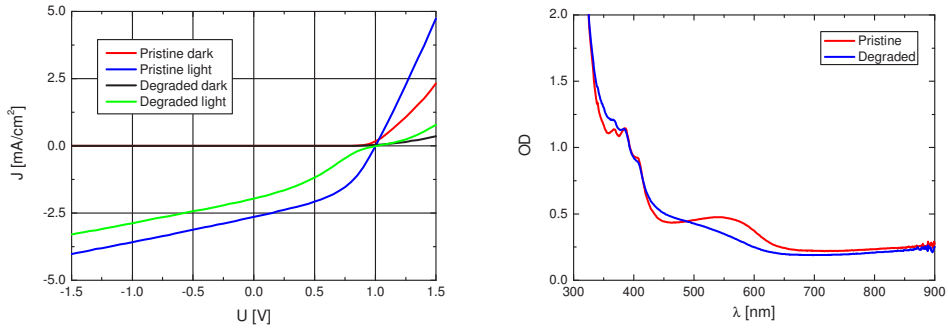

Figure 4.2.4 *JV* characteristics (a) and absorption spectra (b) for a pristine and degraded ITO/PEDOT:PSS/APFO3:PCBM/LiF/Al device.

One possibility to decouple different degradation mechanisms is to study how the individual components behave when exposed to light and ambient conditions, however, this is not always representative of a device under operation. For example the results presented above shows that aluminum is highly sensitive to degradation. However, as seen in Figure 4.2.5 the CELIV and photo-CELIV current transients show no sign of a displacement current due to trapping, the CELIV transient in the dark does not depend on the applied voltage and the *j(0)* corresponds to what is expected from the geometrical capacitance. The photo-

CELIV transients show a slight decrease in the mobility for the degraded device, with around a factor of two ($9{\cdot}10^{-4}$ cm^2/Vs for the pristine and $5{\cdot}10^{-4}$ cm^2/Vs for the degraded device). However, it should be noted that the difference in mobility seen here is on the detection limit of a photo-CELIV experiment (photo-CELIV is accurate to roughly within a factor of two).

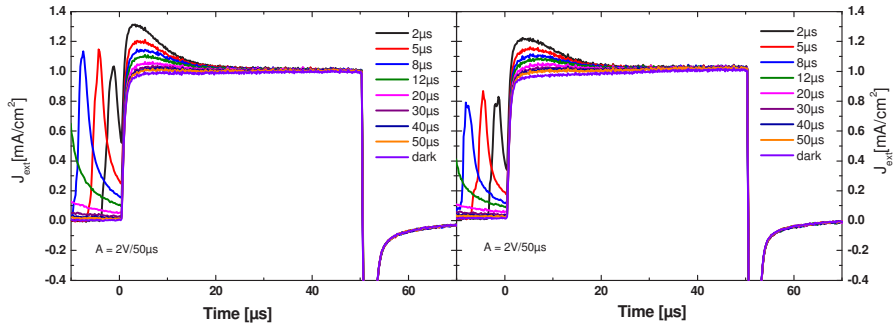

Figure 4.2.5 Photo-CELIV transients of a pristine (a) and degraded (b) ITO/PEDOT:PSS/APFO3:PCBM/LiF/Al device

Another possibility to decouple different degradation mechanisms is to use characterization techniques that are sensitive to changes in only one component, for example the active layer may be optically probed which will exclude the impact of imperfect contacts. The bleaching of the absorption spectra shows that that the active layer has suffered some degradation, however, the information obtained from absorption alone is limited. By performing photo-induced absorption measurements the recombination dynamics and charge carrier lifetimes and can be obtained and compared.

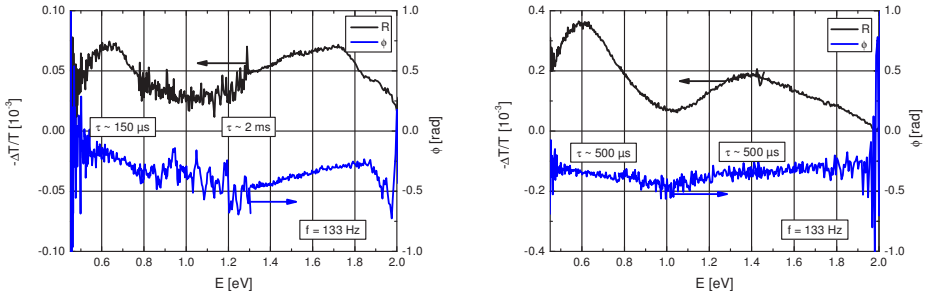

Figure 4.2.6 Radius (R) and phase (φ) of the PA signal of a (a) pristine and (b) degraded APFO3:PCBM film

Figure 4.2.6 shows the radius (R) and phase (φ) of the PA signal of a (a) pristine and (b) degraded APFO3:PCBM film. Clear spectral differences can be seen as a consequence of the degradation. The magnitude of the photo-induced absorption is significantly larger in the degraded case implying a higher density of absorbing species which in turn implies either longer lifetimes or a larger generation of absorbing species in the degraded case. The phase of the pristine device suggests that there are at least two different lifetimes of absorbing species whereas the lifetimes in the degraded film are roughly the same over the whole spectrum. The low energy band peak around 0.6 eV, previously attributed to polarons [105], is more pronounced in the degraded film the corresponding polaron densities being 5.4×10^{16} cm^{-3} in the pristine and 2.7×10^{17} cm^{-3} in the degraded film. Furthermore, the polaron lifetime is considerably longer in the degraded film; 500 μs versus 150 μs in the pristine case. Higher polaron densities and longer lifetimes imply a lower recombination rate in the degraded sample. Furthermore, it is seen from the intensity dependent PA and V_{OC} that the recombination in the degraded case is primarily bimolecular (not shown). Since the bimolecular recombination is directly related to the mobility a lower recombination rate suggests that the charge carrier mobility is lower in the degraded case, in agreement with the photo-CELIV data. However, the differences are in the recorded mobilities are small and it is highly unlikely that the only cause of the s-kink would be unbalanced charge transport, imperfect contacts being the much more likely culprit.

4.2.3. How to differentiate between different contact-related effects leading to reduced performance

As mentioned in section 4.2.2 above, the complexity of the degradation process makes it difficult to discern the main cause of degradation from *JV* measurements alone. Whereas it is challenging to controllably degrade one component in a device to study its impact on the performance, the effects of single isolated degradation mechanisms can be clarified by drift-diffusion simulations, as is demonstrated in Paper IV. In drift-diffusion modeling the properties of each component can be chosen freely and thus provides a way of distinguishing between different effects.

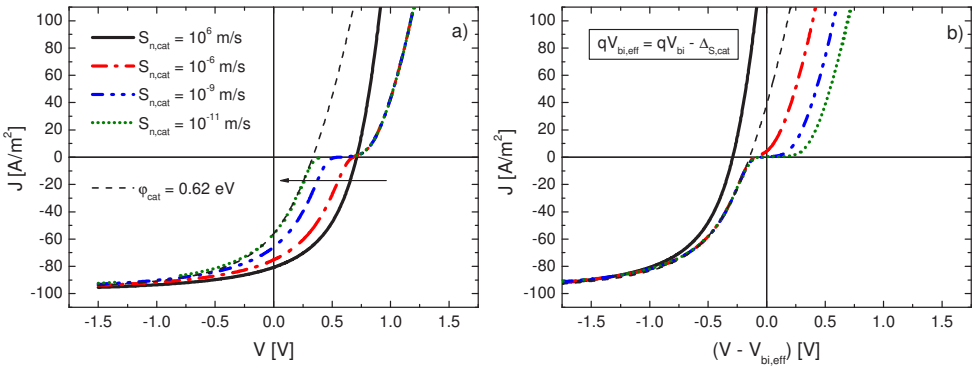

Figure 4.2.7 The effect of reduced surface recombination velocities at the cathode compared to an ideal device. In b) the non-ideal curves are shifted by $\Delta_{S,cat}$.

Figure 4.2.7 a) shows the effect of reduced surface recombination velocities at the cathode compared to an ideal device. The black dashed line is an ideal device but with an injection barrier at the cathode showed for comparison. It can be seen that for voltages well below the V_{OC} the non-ideal JV curves with a reduced surface recombination velocity very closely follows the JV curve of a device with an effectively increased injection barrier but otherwise ideal. The effective increased injection barrier $\Delta_{S,cat}$ is due to an increased diffusion potential of the accumulated charge and is given by:

$$\Delta_{S,cat} = kT \ln\left(1 + \frac{2\mu_n kT}{qS_{n,cat}d}\right) \tag{4.2.2}$$

where $S_{n,cat}$ is the surface recombination velocity for electrons at the cathode. Figure 4.2.7 b) shows the JV curves in a) shifted by $\Delta_{S,cat}$, the curves are seen to overlap nicely with the ideal JV curve in reverse bias. The differing currents in forward bias are caused by the fact that the currents are hole-dominated since a reduced surface recombination velocity reduces electron injection as well as extraction. If the ideal JV curve is not available the distance between the two inflection points may be used as a measure of $\Delta_{S,cat}$. One should note that the inflection points of the s-shaped JVs in Figure 4.2.7 are located very close to the x-axis and the V_{OC} is closely given by the V_{OC} of the ideal device.

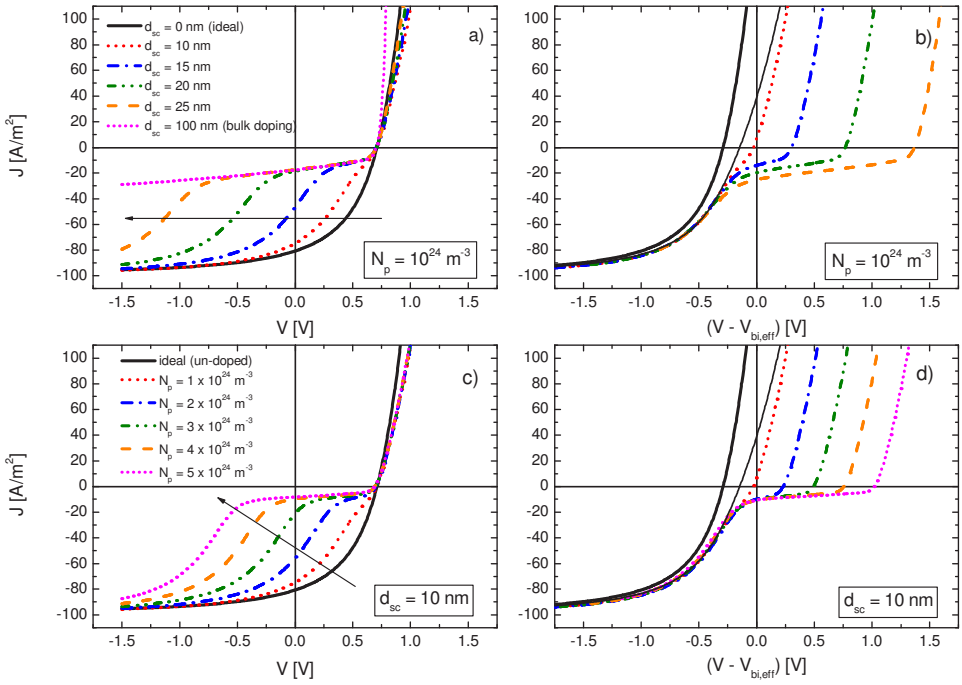

Figure 4.2.8 The effect of a p-doped layer at the cathode for varying layer widths (a) and doping densities (c), in (b) and (d) the curves in (a) and (c) are shifted by $\Delta_{p,cat}$

The effect of interfacial hole doping at the cathode is shown in Figure 4.2.8. Figure 4.2.8 c) shows simulated *JV* curves for increased hole doping density, the width of the doped region is 10 nm. It can be seen that in forward bias and especially far in reverse bias the non-ideal curves closely overlap with the ideal *JV* curve. At moderate reverse bias the current is largely reduced compared to the ideal case; the current in this region corresponds to the current of a device with the same doping density stretching over the whole of the bulk. The s-kink marks the transition between these two regions, the position of the s-kink is dependent on both the width of the doped layer and the doping density. The fixed space charge of the dopants causes band-bending that effectively decreases the built-in voltage; the band-bending being given by:

$$\Delta_{p,cat} = \frac{q^2 N_p d_{sc}^2}{2\varepsilon\varepsilon_0} \qquad (4.2.3)$$

By shifting the non-ideal *JV* curves so that they overlap with the ideal one, as shown in Figure 4.2.8 b), the doping density may be estimated according to Equation 4.2.3 (if the width of the doped layer is known). If an ideal *JV* curve is not available, the band-bending may be approximated by the distance between the two inflection points of the non-ideal *JV* curve. Note that in the case of doping in the vicinity of the contact the inflection point of the s-shape is typically found well below the x-axis.

An s-shaped *JV* may also arise due to trapping of majority carriers in the vicinity of the electrodes. In the case of deep traps, the trapped charges essentially form a fixed space charge as in the case of interfacial doping, and the resulting *JV* curves are very similar. In the case of shallow traps the amount of trapped charges will be voltage dependent and in this case it is difficult to draw any conclusions from a single non-ideal *JV* curve.

Figure 4.2.4 can now be revisited, with the results from drift-diffusion modelling in mind. The V_{OC} of the degraded cell is very close to the pristine one which suggests that the contact work functions are likely unaffected by the degradation. Furthermore, the inflection point is located on the x-axis suggesting that the reason for the s-shaped *JV* is an effectively reduced surface recombination velocity. The decrease in the built-in voltage (and hence the driving force for extraction) induced by the reduced surface recombination velocity may then be approximated by the distance between the inflection points of the degraded *JV* curve.

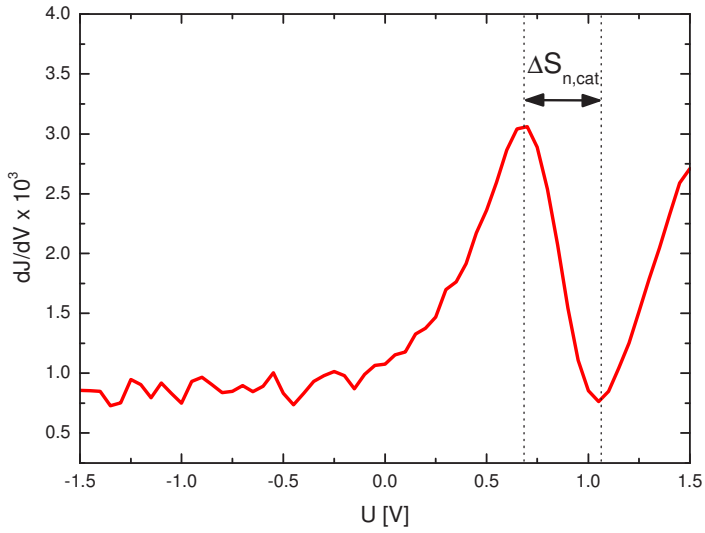

Figure 4.2.9 The derivative of the current in Figure 4.2.4.

Figure 4.2.9 shows the derivative of the current in Figure 4.2.4, the inflection points are the local extrema, $\Delta_{S,cat}$ is approximately 0.4V. The corresponding surface recombination velocity as calculated by Equation 4.2.2 is then on the order of 10^{-9} m/s. The approximation is crude and might very well be off by an order of magnitude. However, $\Delta_{S,cat}$ is over eight orders of magnitude smaller than the charge carrier drift velocity in the bulk ($v_{drift} = \mu F = 0.2$ m/s for $\mu = 5 \cdot 10^{-4}$ cm^2/Vs and $F = 35000$ V/cm), clearly indicating that the contact is limiting.

4.3. Organic-organic interfaces

The donor-acceptor interface is of paramount importance in BHJ solar cells since the light generated excitons can only be separated to free electrons and holes at the interface. Furthermore, the interface also governs the non-geminate charge recombination since this also occurs across the interface. The dominating mechanism of non-geminate recombination in BHJ solar cells is a highly debated matter; SRH type recombination is typically observed in steady-state measurements whereas direct band-to-band recombination is commonly observed in transient measurements.

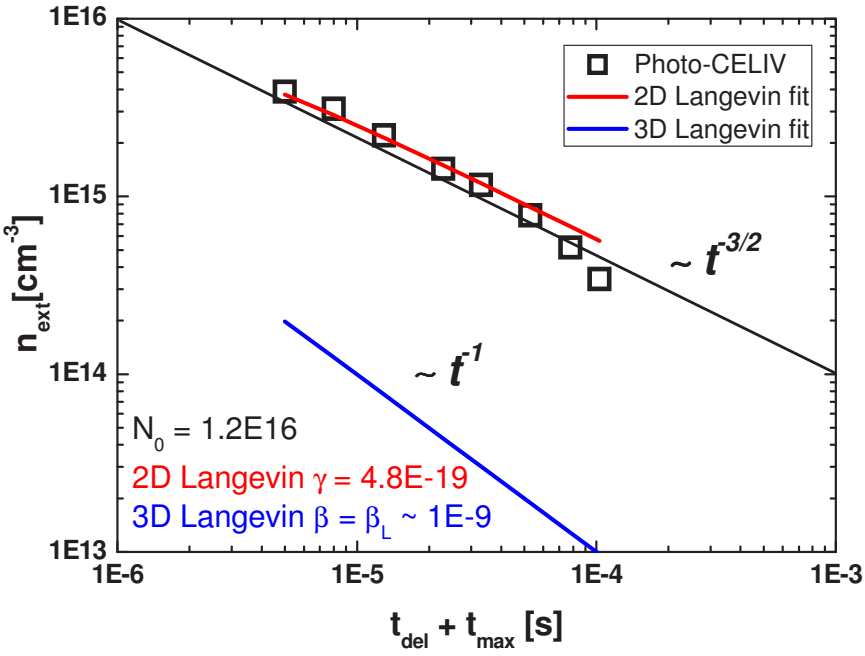

Figure 4.3.1 The density of extracted charge n_{ext} as a function of t_{del} + t_{max} for a PBTTT:PCBM 1:4 device.

Figure 4.3.1 shows the extracted charge n_{ext} as a function of t_{del} + t_{max} from a photo-CELIV experiment of a PBTTT:PCBM 1:4 device. It can be seen that $n_{ext}(t_{del}+t_{max})$ is proportional to $t^{-2/3}$ at long times indicating α = 2.5 i.e 2D-Langevin. PBTTT:PCBM forms a highly ordered lamellar structure and 2D-Langevin is therefore expected. The data can be fitted well to the 2D-Langevin model with N_0 = $1.2{\cdot}10^{16}$ cm^{-3} and γ = $4.8{\cdot}10^{-19}$ $cm^{9/2}s^{-1}$, the corresponding apparent reduction versus

3D-Langevin is roughly 0.03. The data can be fitted reasonably well also with the 3D-Langevin model – provided that $\beta \approx 0.03\beta_L$.

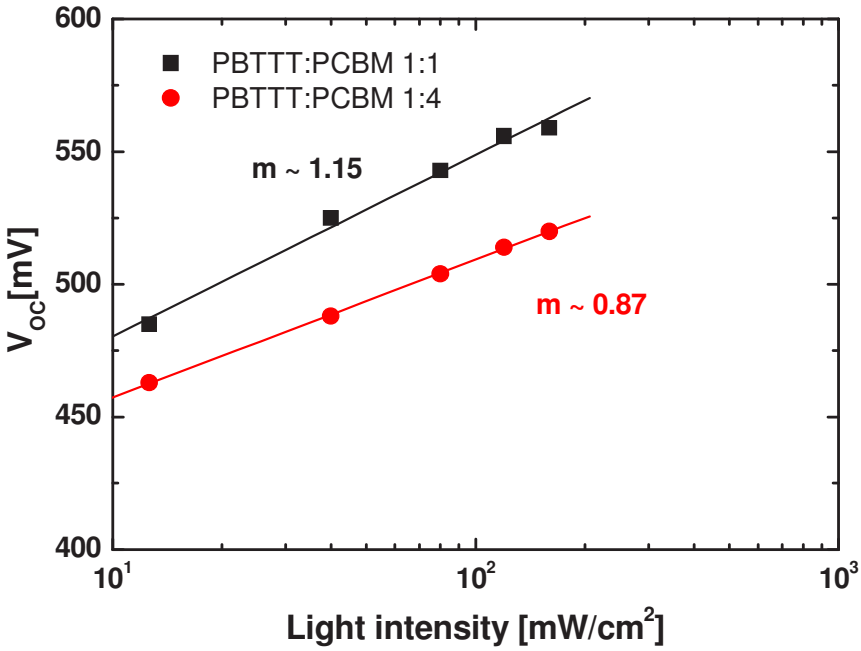

Figure 4.3.2 The V_{OC} as a function of light intensity for a PBTTT:PCBM 1:1 and 1:4 device.

Figure 4.3.2 shows the V_{OC} as a function of light intensity of a PBTTT:PCBM 1:1 and 1:4 device. It can be seen that the light ideality factor in the 1:4 case is ~ 0.87 which is very close to what is expected from 2D-Langevin recombination. In general, the only possibility of having a lower light ideality factor than 1 is if the recombination is of higher order than 2 (assuming Ohmic contacts and moderate light intensities). In the 1:1 case the light ideality factor is considerably higher ~ 1.15 indicative of a higher degree of SRH type recombination. This is in excellent agreement with previous work showing that electrons are more localized in the 1:1 case due to the long inter-site distance [75].

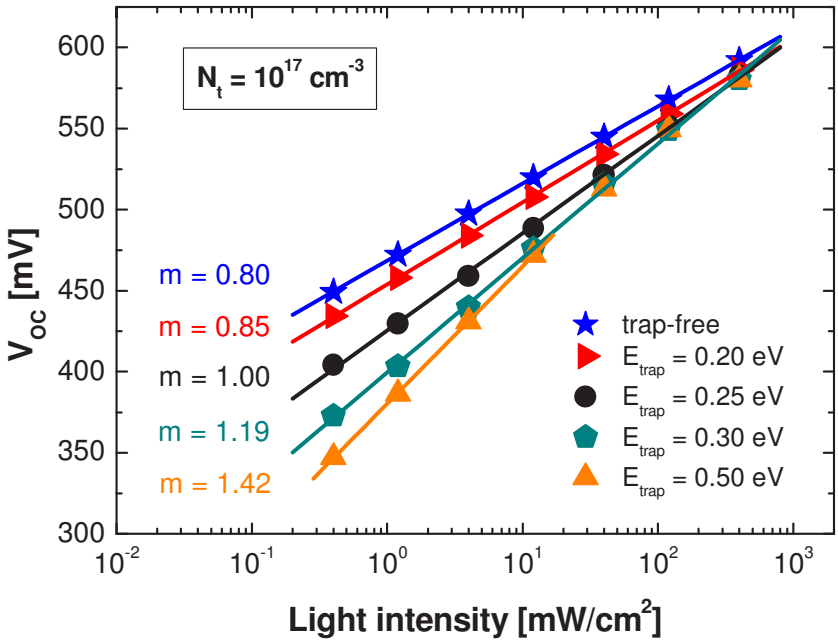

Figure 4.3.3 Simulated light ideality factors m for a 2D-Langevin system with varying trap depths (E_{trap}) for $N_t = 10^{17}$ cm^{-3}, and $C_p = C_{p,2D}$ as per Equation 2.2.9. For simplicity the SRH capture coefficients for electrons and holes were assumed to be equal in the simulations.

Figure 4.3.3 shows simulated V_{OC} as a function of light intensity with varying trap depths. It can be seen that $m = 0.8$ in the trap-free case and gradually increases for increasing trap depths, never exceeding 1.6, however. A similar trend is seen if the trap depth is kept constant and the trap density is gradually increased. This is in agreement with previous findings on P3HT:PCBM showing light ideality factors ranging from 1.2 to 1.6 [55, 106-108]. Wetzelaer et al suggested that since direct bi-molecular recombination is so strongly reduced in P3HT:PCBM (due to 2D-Langevin) the recombination that is observed is highly dominated by SRH [69]. In the PBTTT:PCBM 1:4 case the reduction in the direct bi-molecular recombination is much smaller than in the P3HT:PCBM case due to the fact that the lamellar thickness is larger in the PBTTT:PCBM blend. Furthermore the PBTTT:PCBM 1:4 blend shows high structural and energetic order which leads to an ideality factor approaching 0.8 [75].

5. Summary

The effect of interfaces in organic electronic devices becomes ever more important, and in order to further advance the field of organic electronics, and OPV in particular, careful control of the relevant interfaces is needed. This thesis deals with interfacial effects at metal-organic and organic-organic interfaces in organic diodes and solar cells. The measurement techniques employed are not in themselves surface-sensitive but by modifying the interfacial properties in different ways significant changes can be seen also using techniques that measure the properties of the bulk of the active layer or the whole device. This is in itself evidence of the importance of interfaces. Furthermore, it is shown that the PCE of OPV devices depends directly on the properties of the metal-organic and organic-organic interfaces.

Results on metal-organic interfaces show that non-ideality of contacts result in weakened performance. The effect of trap states in AlO_x is clarified in Paper II; it is shown that trap states in thin dielectrics give rise to a large displacement current due to trap filling, which slows down device operation. A high density of trap states will also cause gate leakage in transistors due to trap-assisted charge transport. The large displacement current is utilized to determine the vacuum level shifts caused by modifying the AlO_x with SAMs. The exact mechanism leading to the vacuum dipole shift is still not entirely clear; the observed dipole shifts do not scale with the dipole moments of the individual molecules.

In paper III it is shown that a solar cell that has been exposed to ambient conditions and simulated sunlight suffers from reduced performance due to an s-shaped *JV* curve. Degradation affects both the active layer and the contacts, however, by using the results from Paper IV it can be concluded that the cause of the s-shape is a reduced surface recombination velocity. In Paper IV the effect of non-ideal on contacts the *FF* in organic solar cells is clarified. Reduced surface recombination velocities, doping and trapping in the vicinity of the contacts is shown to give rise to distinctively different s-shapes, providing a way of distinguishing between different effects. Some results relating the non-ideality of contacts to the V_{OC} are also presented, however, this could be extended further to include the effect of recombination and doping on the V_{OC}.

Also seemingly ideal contacts might limit performance depending on the interfacial properties as was shown in Paper I. Spontaneous charge transfer across the metal-organic interface cause band-bending which limits the maximum attainable V_{OC}, the amount of transferred charge depends on the energy levels and densities of discrete interfacial states.

Results on organic-organic interfaces (Paper V) show that charge recombination is governed by the ordering of the donor and acceptor phases and the interface between them. When the acceptor and donor are ordered in a completely intermixed phase the recombination rate is higher than if the intermixed phases are surrounded by pure domains. The 2D-Langevin formalism is extended to the case with a high density of trap states. It is shown that in lamellar systems the recombination rate is reduced compared to more disordered systems both in the case of direct bi-molecular recombination and trap-assisted recombination.

Svensk Resumé

Solceller baserade på organiska halvledare erbjuder en möjlighet till storskalig och billig solenergiproduktion. Organiska halvledare har den fördelen att de är lösningsprocesserbara vilket gör att solceller och andra elektroniska komponenter baserade på dessa halvledare kan tillverkas vid låga temperaturer och med liten energiförbrukning. Nackdelen med dessa material är deras strukturella och energetiska oordning som leder till att solceller bestående av endast en halvledare är mycket ineffektiva. För att effektivt kunna omvandla ljus till elektricitet med organiska solceller krävs två olika halvledare, en donor och en acceptor. Även med denna donor-acceptorstruktur har organiska solceller lägre effektivitet än sådana solceller som är baserade på oorganiska halvledare vilket dels beror på att rekombinationen, som är en förlustmekanism, är större i oorganiska material.

För att organiska solceller ska kunna kommersialiseras krävs grundläggande insikter i de elektrooptiska processer som gör att ett flöde av fotoner omvandlas till elektricitet. En stor del av forskningen om dessa elektrooptiska processer har varit fokuserad kring egenskaperna av de aktiva materialen som sådana, medan gränsytorna mellan olika material har fått mindre uppmärksamhet. Gränsytor mellan olika material har distinkt olika egenskaper jämfört med ett rent material, och gränsytors olika egenskaper kan ha en väldigt stor inverkan på hur solcellerna fungerar. Syftet med denna avhandling är att klargöra några olika gränsyterelaterade effekter i organiska dioder och solceller. De gränsytor som behandlas är gränsytan mellan kontakten och det aktiva lagret (metall-organisk) och gränsytan mellan donor och acceptor (organisk-organisk). De mätmetoder som används är ström-spänningskarakterisering, transient laddningsextraktion och fotoinducerad absorption. Metoderna är i sig inte ytkänsliga men genom att modifiera gränsytorna på olika sätt kan man åstadkomma märkbara förändringar också med relativt enkla metoder som de ovannämnda. De experimentella metoderna kompletteras med datorsimuleringar som modellerar laddningars drift och diffusion i det aktiva lagret, samt extraktion vid kontakterna.

Resultaten visar att metall-organiska gränsytor måste designas noggrant för att begränsa förlust av effektivitet. En icke-idealisk kontakt leder till strakt reducerad effektivitet på grund av s-formade ström-spänningskurvor. Även till synes idealiska kontakter kan orsaka förluster genom spontan laddningsöverföring från metallen till det organiska lagret som effektivt sett minskar på den spänning som cellen kan alstra. Den organisk-organiska gränsytan påverkar hur mycket ström cellen kan alstra och beroende på gränsytans beskaffenhet kan de negativa rekombinationsprocesserna i materialet kontrolleras.

References

[1] H. Sirringhaus, *Adv. Mater.* **26**, 1319 (2014)

[2] L. Torsi, M. Magliulo, K. Manolia, and G. Palazzoa, *Chem. Soc. Rev.* **42**, 8612 (2013)

[3] G. G. Malliaras, *Biochimica et Biophysica Acta* **1830,** 4286 (2013)

[4] O. Inganäs, and S. Admassie, *Adv. Mater.* **26**, 830 (2014)

[5] S. Braun, W. R. Salaneck, and M. Fahlman, *Adv. Mater.* **21**, 1450-1472 (2009)

[6] D. M. Chapin, C. S. Fuller, and G. L. Pearson, *J. Appl. Phys.* **25**, 676 (1954)

[7] W. Shockley and H. J. Queisser, *J. Appl. Phys.* **32**, 510 (1961)

[8] C. Deibel, and V. Dyakonov, *Rep. Prog. Phys.* **73**, 096401 (2010)

[9] C. W. Tang, *Appl. Phys. Lett* **48**, 183 (1986)

[10] G. Yu, J. Gao, J. C. Hummelen, F. Wudl, and A. J. Heeger, *Science* **270**, 1789 (1995)

[11] M. Campoy-Quiles, T.Ferenczi, T.Agostinelli, P.G. Etchegoin, Y.Kim, T.D. Anthopoulos, P.N. Stavrinou, D.D. C. Bradley, and J. Nelson, *Nature Mater.* **7**, 158 (2008)

[12] R. A. J. Janssen, and J. Nelson, *Adv. Mater.* **25**, 1847 (2013)

[13] L. J. A. Koster, S. E. Shaheen, and J. C. Hummelen, *Adv. Ener. Mater.* **2**, 1246 (2012)

[14] W. Tress, K. Leo, and M. Riede, *Phys. Rev. B* **85**, 155201 (2012)

[15] M. C. Scharber, D. Mühlbacher, M. Koppe, P. Denk, C. Waldauf, A. J. Heeger, C. L. Brabec, *Adv. Mater.* **18**, 789 (2006)

[16] K. Vandewal, K. Tvingstedt, A. Gadisa, O. Inganäs, J. V. Manca, *Nature Mater.* **8**, 904 (2009)

[17] M. Hallermann, I. Kriegel, E. Da Como, J. M. Berger, E. Von Hauff, J. Feldmann, *Adv. Funct. Mater.* **19** 22 3662 (2009)

[18] A. Wagenpfahl, D. Rauh, M. Binder, C. Deibel, and V. Dyakonov, *Phys. Rev. B* **82**, 115306 (2010)

[19] W. Tress, K. Leo, and M. Riede, *Adv. Funct. Mater.* **21**, 2140–2149 (2011)

[20] W. Tress, S. Corvers, K. Leo, and M. Riede, *Adv. Energy Mater.* **3**, 873–880 (2013)

[21] M. Jørgensen, K. Norrman, and F. C. Krebs, *Solar Energy Mater. & Solar Cells* **92**, 686–714 (2008)

[22] M. Jørgensen, K. Norrman, S. A. Gevorgyan, T. Tromholt, B. Andreasen, and F. C. Krebs, *Adv. Mater.* **24**, 580–612 (2012)

[23] J. D. Kotlarski, D. J. D. Moet, and P. W. M. Blom, *Polymer Physics* **49**, 708 (2011)

[24] B. T. De Villers, C. J. Tassone, S. H. Tolbert, and B. J. Schwartz, *J. Phys. Chem. C* **113**, 18978 (2009)

[25] A. Seemann, T. Sauermann, C. Lungenschmied, O. Armbruster, S. Bauer, H.-J. Egelhaaf, and J. Hauch, *Solar Energy* **85** (2011) 1238–1249

[26] I. Lange, J. C. Blakesley, J. Frisch, A. Vollmer, N. Koch, and D. Nehar, *Phys. Rev. Lett.* **106,** 216402 (2011)

[27] Z. Xu, L-M Chen, M-H Chen, G. Li, and Y. Yang, *Appl. Phys. Lett.* **95**, 013301 (2009)

[28] Z.-L. Guan, J. B. Kim, H. Wang, C. Jaye, D. A. Fischer, Y.-L. Loo, and Antoine Kahn, *Org. El.* **11**, 1779 (2010)

[29] H. Aarnio, P. Sehati, S. Braun, M. Nyman, M. P. De Jong, M. Fahlman, and R. Österbacka, *Adv. Ener. Mat.* **1**, 792 (2011)

[30] H. Aarnio, and R. Österbacka, *Energy Procedia* **31**, 21 (2012)

[31] Q. Bao, O. Sandberg, D. Dagnelund, S. Sandén, S. Braun, H. Aarnio, X. Liu, W. M. Chen, R. Österbacka, and M. Fahlman, *Adv. Funct. Mater.* **24**, 40, 6309 (2014)

[32] A.-E. Haj-Yahia, O. Yaffe, T. Bendikov, H. Cohen, Y. Feldman, A. Vilan, and D. Cahen, *Adv. Mater.* **25**, 702-706 (2013)

[33] Z. Li, J. Li, and X. Luo, *Applied Surface Science* **282**, 487-491 (2013)

[34] F. D. Fleischli, S. Suárez, M. Schaer, and L. Zuppiroli, *Langmuir* **26**, 18, 15044 (2010)

[35] J. F. Martínez Hardigree, T. J. Dawidczyk, R. M. Ireland, G. L. Johns, B.-J. Jung, M. Nyman, R. Österbacka, N. Marković, and H. E. Katz, *ACS Appl. Mater. Interfaces* **5**, 7025 (2013)

[36] H. Kim, Z. Meihui, N. Battaglini, P. Lang, and G. Horowitz, *Organic Electronics* **14**, 2108-2113 (2013)

[37] M. Song, J.-W. Kang, D.-H. Kim, J.-D. Kwon, S.-G. Park, S. Nam, S. Jo, S. Y. Ryu, and C. S. Kim, *Appl. Phys. Lett.* **102**, 143303 (2013)

[38] J.-M. Chiu, and Yian Tai, *ACS Appl. Mater. Interfaces* **5**, 6946-6950 (2013)

[39] O. L. A. Monti, *Phys. Chem. Lett.* **3**, 2342-2351 (2012)

[40] L. Onsager, *J. Chem. Phys.* **2**, 599 (1934)

[41] C. L. Braun, *J. Chem. Phys.* **80**, 4157 (1984)

[42] M. Pope and C. E. Swenberg, *Electronic Processes in Organic Crystals and Polymers*, 2nd ed. (Oxford University Press, New York, 1999), p. 460

[43] M. P. Langevin, *Ann. Chim. Phys.,* **28**:433 (1903)

[44] M. Kuik, G.-J. A. H. Wetzelaer, H. T. Nicolai, N. I. Craciun, D. M. de Leeuw, and P. W. M. Blom, *Adv. Mater.* **26**, 512-531 (2014)

[45] A. Pivrikas, G. Juška, A. J. Mozer, M. Scharber, K. Arlauskas, N. S. Sariciftci, H. Stubb, and R. Österbacka, *Phys. Rev. Lett.* **94**, 176806 (2005)

[46] T. M. Clarke, D. B. Rodovsky, A. A. Herzing, J. Peet, G. Dennler, D. DeLongchamp, C. Lungenschmied, and A. J. Mozer, *Adv. Energy Mater.* **1**, 1062 (2011)

[47] D. H. K. Murthy, A. Melianas, Z. Tang, G. Juska, K. Arlauskas, F. Zhang, L. D. A. Siebbeles, O. Inganäs, and T. J. Savenije, *Adv. Funct. Mater.* **23** 34, 4262-4268 (2013)

[48] C. Deibel, A. Wagenpfahl, and V. Dyakonov, *Phys. Rev. B* **80**, 075203 (2009)

[49] A. Pivrikas, N. S. Sariciftci, G. Juška, and R. Österbacka, *Prog. Photovolt: Res. Appl.* **15** (2007) 677-696

[50] L. J. A. Koster, V. D. Mihailetchi, and P. W. M. Blom, *Appl. Phys. Lett.* **88** 5, 052104 (2006)

[51] C. Groves, and N. C. Greenham, *Phys. Rev. B* **78**, 155205 (2008)

[52] L. J. A. Koster, E. C. P. Smits, V. D. Mihailetchi, and P. W. M. Blom, *Phys. Rev. B* **72**, 085205 (2005)

[53] C. G. Shuttle, B. O'Regan, A. M. Ballantyne, J. Nelson, D. D. C. Bradley, J. de Mello, and J. R. Durrant, *Appl. Phys. Lett.* **92**, 09331 (2008)

[54] G. Juška, K. Genevičius, N. Nekrašas, G. Sliaužys, and G. Dennler, *Appl. Phys. Lett.* **93**, 143303 (2008)

[55] T. Kirchartz, B. E. Pieters, J. Kirkpatrick, U. Rau, and J. Nelson, *Phys. Rev. B* **83**, 115209 (2011)

[56] T. Kirchartz, and J. Nelson, *Phys. Rev. B* **86** 165201 (2012)

[57] R. A. Street, A. Krakaris, and S. R. Cowan, *Adv. Funct. Mater.* **22**, 4608 (2012)

[58] G. Juška, K. Genevičius, N. Nekrašas, G. Sliaužys, and R. Österbacka, *Appl. Phys. Lett.* **95**, 013303 (2009)

[59] R. Österbacka, A. Pivrikas, G. Juška, A. Poskus, H. Aarnio, G. Sliaužys, K. Genevičius, K. Arlauskas, and N. S. Sariciftci, *IEEE J. Sel. Top. Quantum Electron.* **16**, 1738 (2010)

[60] H. Sirringhaus, P. J. Brown, R. H. Friend, M. M. Nielsen, K. Bechgaard, B. M. W. Langeveld-Voss, J. H. Spiering, R. A. J. Janssen, E. W. Meljer, P. Herwig, and D. M. de Leeuw, *Nature* **401**, 685 (1999)

[61] J. Gorenflot, M. C. Heiber, A. Baumann, J. Lorrmann, M. Gunz, A. Kämpgen, V. Dyakonov, and C. Deibel, *J. Appl. Phys.* **115**, 144502 (2014)

[62] G. Juška, K. Genevičius, N. Nekrašas, and G. Sliaužys, *Phys. Status Solidi C* **7** 3-4, 980 (2010)

[63] M. Nyman, unpublished

[64] Y. He, and Y. Li, *Phys. Chem. Chem. Phys.* **13**, 1970 (2011)

[65] J. C. Hummelen, B. W. Knight, F. Lepeq, and F. Wudl, *J. Org. Chem.* **60**, 532 (1995)

[66] M. Brinkmann, P. Rannou, *Adv. Funct. Mater.* **17**, 101-108 (2007)

[67] M. T. Dang, M. Hirsch, and G. Wantz, *Adv. Mater.* **23**, 3597 (2011)

[68] M. Pfannmöller, H. Flügge, G. Benner, I. Wacker, C. Sommer, M. Hanselmann, S. Schmale, H. Schmidt, F. A. Hamprecht, T. Rabe, W. Kowalsky, and R. R. Schröder, *Nano Lett.* **11**, 3099-3107 (2011)

[69] G. A. H. Wetzelaer, M. Kuik, and P. W. M. Blom, *Adv. Energy Mater.* **2**, 10, 1232–1237 (2012)

[70] O. Inganäs, M. Svensson, F. Zhang, A. Gadisa, N. K. Persson, X. Wang, M. R. Andersson, *Applied Physics A* **79**, 31-35 (2004)

[71] O. Inganäs, F. Zhang, and M. Andersson, *Acc. Chem. Res.*, **42,** 1731–1739 (2009)

[72] A. C. Mayer, M. F. Toney, S. R. Scully, J. Rivnay, C. J. Brabec, M. Scharber, M. Koppe, M. Heeney, I. McCulloch, and M. McGehee, *Adv. Funct. Mater.* **19**, 1173-1179 (2009)

[73] Nichole C. Cates, Roman Gysel, Zach Beiley, Chad E. Miller, Michael F. Toney, Martin Heeney, Iain McCulloch, and Michael D. McGehee, *Nano Letters* **9** 12, 4153-4157 (2009)

[74] W.L. Rance, A. J. Ferguson, T. McCarthy-Ward, M. Heeney, D. S. Ginley, D. C. Olson, G. Rumbles, and N. Kopidaki, *ACS Nano* **5** (2011) 5635–5646

[75] M. Nyman, O. J. Sandberg, R. Österbacka, submitted.

[76] B. J. Jung, J. Sun, T. Lee, A. Sarjeant, and H. Katz, *Chem. Mater.* **21**, 94-101 (2009)

[77] B. J. Jung, K. Lee, J. Sun, A. G. Andreou, and H. Katz, *Adv. Funct. Mater.* **20**, 2930-2944 (2010)

[78] M. F. Calhoun, J. Sanchez, D. Olaya, M. E. Gershenson, and V. Podzorov, *Nature Materials* **7**, 84 (2008)

[79] D. J. Ellison, B. Lee, V. Podzorov, and C. D. Frisbie, *Adv. Mater.* **23**, 502–507 (2011)

[80] M. Wang, F. Xie, J. Du, Q. Tang, S. Zheng, Q. Miao, J. Chen, N. Zhao, and J. B. Xu, *Solar Energy Mater. & Solar* Cells **95**, 12 3303 (2011)

[81] T. W. Hickmott, *J. Appl. Phys.* **87,** 11, 7903-7912 (2000)

[82] J. R. Weber, A. Janotti, and C. G. Van de Walle, *J. Appl. Phys.* **109,** 033715 (2011)

[83] G. Juška, K. Arlauskas, M. Viliūnas, and J. Kocka, *Phys. Rev. Lett.* **84**, 4946 (2000)

[84] G. Juška, K. Arlauskas, M. Viliūnas, K. Genevičius, R. Österbacka, and H. Stubb, *Phys. Rev. B* **62**, 16 235 (2000)

[85] G. Juška, M. Viliūnas, K. Arlauskas, N. Nekrašas, N. Wyrsch, and L. Feitknecht, *J. Appl. Phys.* **89**, 4971 (2001)

[86] R. Österbacka, A. Pivrikas, G. Juška, K. Genevičius, K. Arlauskas, and H. Stubb, *Current Appl. Physics* **4**, 534 (2004)

[87] S. Sandén, O. Sandberg, Q. Xu, J.-H. Smått, G. Juška, M. Lindén, and R. Österbacka

Phys. Chem. Chem. Phys. **14**, 14186-14189 (2012)

[88] A. Armin, M. Velusamy, P. L. Burn, P. Meredith, and A. Pivrikas, *Appl. Phys. Lett.* **101**, 083306 (2012)

[89] O. J. Sandberg, M. Nyman, and R. Österbacka, *Org. Electron.* 15 (2014) 3413

[90] A. Pivrikas, N. S. Sariciftci, G. Juška, and R. Österbacka, *Prog. Photovolt: Res. Appl.* **15** (2007) 677-696

[91] A. Pivrikas, "Charge Transport and Recombination in Bulk-Heterojunction Solar Cells", Ph.D. thesis, Åbo Akademi University (2006)

[92] J. Lorrmann, B. H. Badada, O. Inganäs, V. Dyakonov, and C. Deibel, *J. Appl. Phys.* **108**, 113705 (2010)

[93] G. Juška, N. Nekrašas, V. Valentinavičius, P. Meredith, and A. Pivrikas, *Phys. Rev. B* **84** (2011) 155202

[94] Z. V. Vardeny, X. Wei, "Optical Probes of Photoexcitations in Conducting Polymers" In: Skotheim TA, Elsenbaumer RL, Reynolds JR, editors. Handbook of Conducting Polymers, New York: Marcel Dekker Inc;1998, p. 639

[95] H. Aarnio, "Photoexcitation dynamics in organic solar cell donor/acceptor systems", Ph.D. thesis, Åbo Akademi University (2012)

[96] W. Tress, K. Leo, and M. Riede, *Appl. Phys. Lett.* **102**, 163901 (2013)

[97] L. J. A. Koster, V. D. Mihailetchi, R. Ramaker, and P. W. M. Blom, *Appl. Phys. Lett.* **86**, 123509 (2005).

[98] T. Kirchartz, F. Deledalle, P. S. Tuladhar, J. R. Durrant, and J. Nelson, *J. Phys. Chem. Lett.* **4** 2371-2376 (2013)

[99] O. J. Sandberg et al, in preparation.

[100] R. MacKenzie, T. Kirchartz, G. F. A. Dibb, and J. Nelson, *J. Phys. Chem. C* **115**, 9806 (2011)

[101] S. Selberherr, Analysis and Simulation of Semiconductor Devices (Springer-Verlag, Wien, 1984)

[102] H. K. Gummel, *IEEE Trans. Electron. Devices* **11**, 455 (1964)

[103] D. L. Scharfetter, and H. K. Gummel, *IEEE Trans. Electron. Devices* **16**, 64 (1969)

[104] M. Girtan, and M. Rusu, Solar Energy Materials & Solar Cells 94, 446 (2010)

[105] H. Aarnio, M. Westerling, R. Österbacka, M. Svensson, M. R. Andersson, T. Pascher, J. Pan, V. Sundström, and H. Stubb, *Synth. Met.* **155**, 299 (2005)

[106] T. Tromholt, M. V. Madsen, and F. C. Krebs, *Appl. Phys. Lett.* **102**, 123904

(2013)

[107] A. Foertig, J. Rauh, V. Dyakonov, and C. Deibel, *Phys. Rev. B* **86**, 115302 (2012)

[108] M. Lenes, S. W. Shelton, A. B. Sieval, D. F. Kronholm, J. C. Hummelen, and P. W. M. Blom, *Adv. Funct. Mater.* **19**, 3002 (2009)

ISBN 978-952-12-3169-8